



**CENTRO DE INVESTIGACIÓN Y DE ESTUDIOS AVANZADOS  
DEL INSTITUTO POLITÉCNICO NACIONAL**

Unidad Mérida

**DEPARTAMENTO DE FÍSICA APLICADA**

**Polaronic effects in cuprate superconductors from a three-sites  
Peierls-Hubbard model**

Thesis presented by:

**Andrés García Saravia Ortíz de Montellano**

To obtain the degree of:

**Doctor of Sciences**

In

**Applied Physics**

Thesis Director:

**Dr. José Mustre de León.**

Mérida, Yucatán, México.

November, 2014





**CENTRO DE INVESTIGACIÓN Y DE ESTUDIOS AVANZADOS  
DEL INSTITUTO POLITÉCNICO NACIONAL**

Unidad Mérida

**DEPARTAMENTO DE FÍSICA APLICADA**

**Efectos polarónicos en superconductores basados en cobre a partir de un  
modelo Peierls-Hubbard de tres sitios.**

Tesis presentada por:

**Andrés García Saravia Ortíz de Montellano**

Para obtener el grado de:

**Doctor en Ciencias**

En

**Física Aplicada**

Director de tesis:

**Dr. José Mustre de León.**

Mérida, Yucatán, México.

November, 2014



# Contents

<b>Contents</b>	<b>I</b>
<b>Aknowledgments</b>	<b>III</b>
<b>Resumen</b>	<b>V</b>
<b>Abstract</b>	<b>VII</b>
<b>Objective</b>	<b>IX</b>
<b>Foreword</b>	<b>XI</b>
<b>1 Introduction</b>	<b>1</b>
1.1 Overview . . . . .	1
1.2 Dynamic local lattice and electronic inhomogeneities . . . . .	5
1.3 Specific heat . . . . .	9
1.4 Electric resistivity . . . . .	10
1.5 Isotopic effects . . . . .	10
<b>2 Peierls-Hubbard model</b>	<b>13</b>
2.1 Hamiltonian and basis set . . . . .	14
2.2 Lattice distortions . . . . .	16
2.3 Charge localization . . . . .	19
2.4 Isotopic substitutions . . . . .	19
2.5 Isotopic shifts . . . . .	23
2.6 Choice of parameters . . . . .	24
<b>3 Cluster distortion and bipolaron formation</b>	<b>27</b>
3.1 Cu(1)-O(4) local distortion . . . . .	28

3.2	Bipolaron binding energy . . . . .	30
<b>4</b>	<b>Infrared spectra</b>	<b>33</b>
4.1	Classification of the excitations . . . . .	33
4.2	Infrared spectra . . . . .	35
4.3	Isotopic shifts . . . . .	36
4.4	Projection into phonon coordinates . . . . .	38
<b>5</b>	<b>Electronic excitations</b>	<b>41</b>
5.1	Partial charge localization . . . . .	43
5.2	Projection into phonon coordinates . . . . .	43
5.3	Isotopic shift . . . . .	44
<b>6</b>	<b>Discussion and conclusions</b>	<b>47</b>
6.1	Validity of the Born-Oppenheimer approximation . . . . .	47
6.2	Multicomponent superconductivity . . . . .	48
	<b>Appendix A Computational details</b>	<b>51</b>
A.1	Algorithm . . . . .	51
A.2	Convergence . . . . .	52
A.3	Numerical instabilities . . . . .	52
	<b>Bibliography</b>	<b>63</b>
	<b>List of figures</b>	<b>64</b>

## Agradecimientos

- Al Conacyt por la beca otorgada durante estos cuatro años de doctorado.
- A mis papás y mis hermanas por todo su apoyo aún en la distancia.
- Al Dr. José Mustre no sólo por ser un excelente asesor de tesis sino por el interés personal que toma en el bienestar de sus alumnos.
- A todos los profesores del Cinvestav Mérida con los que tuve oportunidad de convivir por sus enseñanzas.
- Al personal administrativo del Cinvestav que, en mi experiencia, siempre apoya con gusto y una sonrisa.
- A la comunidad de software libre por la enorme cantidad de herramientas que hicieron posible este trabajo.





## Resumen

En este trabajo revisamos la evidencia de la existencia de distorsiones dinámicas en la red cristalina de superconductores basados en cobre. La presencia de estas distorsiones está relacionada con excitaciones polarónicas. Usando un modelo simple con un hamiltoniano de Peierls-Hubbard mostramos que, para valores intermedios del acoplamiento electrón-red, la representación en espacio real del primer estado excitado reproduce las distorsiones dinámicas observadas debajo de la temperatura de aparición del pseudogap  $T^*$ . Las energías de los estados excitados predecidas por este modelo muestran efectos isotópicos muy diferentes dependiendo de la naturaleza del estado excitado. Estas diferencias pueden explicar los resultados conflictivos obtenidos por diferentes técnicas, ya que éstas exploran diferentes excitaciones en la fase del pseudogap. La plausibilidad de interpretar el estado base del pseudogap como una mezcla inhomogénea de regiones con portadores bipolarónicos y partículas tipo fermiones quasi-libres a partir de los cuales la superconductividad emerge a  $T_c$  es discutida.



## Abstract

Evidence for the existence of local dynamical lattice distortions in cuprates in the pseudogap region of the phase diagram is reviewed. The presence of these distortions is related to polaronic excitations. Using a simple Peierls-Hubbard Hamiltonian we show that, for intermediate values of the electron-lattice coupling, the real space representation of the first excited state reproduces the observed local lattice distortions below the pseudogap appearance temperature,  $T^*$ . The excited state energies predicted by the model exhibit very different isotopic effects depending on the nature of the particular excited state. These differences can explain conflicting results obtained with different techniques, as these probe different excitations of the pseudogap phase. The plausibility of interpreting the pseudogap ground state as an inhomogeneous mixture of nanoscale regions of bipolaronic carriers and quasi-free fermion like particles from which the superconducting state arises at  $T_c$  is discussed.



## Objective



## Foreword

One of the core principles in the scientific endeavour is reproducibility. However, ensuring it is becoming more difficult as a result large data sets generated by complex instruments or algorithms often inaccessible to any scholar other than the original author.

In this spirit I try to make this thesis as reproducible as possible by making accessible the raw datasets as well as the algorithm that produced them in a web repository accessible in this url: <https://github.com/andresgsaravia/PhD-thesis>

Reproducibility is a workflow issue.





# Chapter 1

## Introduction

### 1.1 Overview

Although high temperature superconductivity has been known for almost three decades [1], a satisfactory explanation of this phenomenon still remains as one of the major unsolved problems in theoretical condensed matter physics. The discovery of superconductivity in the ceramic copper oxides was a surprising result since ceramic materials are typically insulators. However, when copper oxides are doped they can become poor metals and superconductors with a high transition temperature  $T_c$  (See Figure 1.1). The doping is provided either by chemical substitution (e.g. in  $\text{La}_{2-x}\text{Sr}_x\text{CuO}_4$  [2]) or by changing the oxygen content (as in  $\text{YBa}_2\text{Cu}_3\text{O}_{7-\delta}$  [3]). Doping leads to the appearance of carriers in the  $\text{CuO}_2$  planes which can be either electrons or holes. Increasing the carrier concentration leads to conductivity and, for larger carrier concentrations, to superconductivity. The value of  $T_c$  depends strongly on the carrier concentration and there is characteristic value of carrier concentration that leads to a maximum  $T_c$  such that larger values of doping concentration produce a decrease in  $T_c$ .

Since electrons must be bound together to form Cooper pairs, it was unexpected to find strong electron-electron correlations in copper oxide superconductors. One example is given by  $\text{La}_2\text{CuO}_4$  which is an insulating material and becomes superconducting, with holes as charge carriers, by replacing some of the trivalent  $\text{La}^{3+}$  in with the divalent  $\text{Sr}^{2+}$ . Band-structure calculations based on the local-density approximation predict the undoped parent compound  $\text{La}_2\text{CuO}_4$  to be metallic but it is found to be an antiferromagnetic insulator [5]. This discrepancy is a consequence of the failure of the independent-particle picture assumed in band-structure calculations and suggests that the undoped parent compounds of the cuprate superconductors are

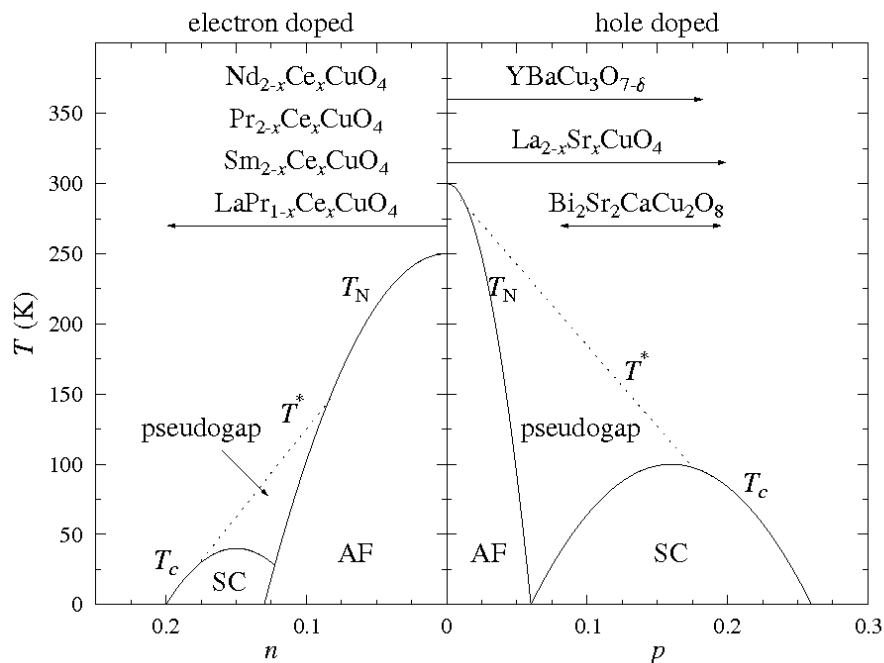


Figure 1.1: Simplified version of the cuprate superconductor phase diagram [4].

*Mott-Hubbard insulators* [6]. That is, the insulating properties are due to strong electron-electron interactions which, nonetheless allow charge to be bound in Cooper pairs in the superconducting state achieved by doping.

Another remarkable feature of the cuprate high-temperature superconductors is the temperature dependence of the normal state resistivity. In optimally doped materials resistivity shows a linear variation with temperature from  $T_c$  to high temperatures (600-1000K) extrapolating to zero resistance at zero degrees [7]. In contrast, conventional metals show a resistivity linearly dependent on temperature only for a limited range of temperatures, have an intercept on the temperature axis at some value greater than zero and saturate at high temperatures [5]. The dependence of the resistivity with temperature is different depending on the doping. We provide a more detailed review later in this introductory chapter (section 1.4) but we emphasize that these resistivity measurements in the (poor) metal phase of the copper oxides differ from what is expected in a normal (Fermi-liquid<sup>1</sup>) metal. These measurements also

<sup>1</sup>Fermi-liquid theory describes the excitations in terms of an interacting gas of renormalized quasiparticles.

indicate a failure of the single-particle picture and suggests the non-applicability of Fermi-liquid theory [8].

One of the defining properties of a superconductor, within the band energy approximation, is the presence of an energy gap, but early experiments could not find this characteristic signature in cuprate superconductors. Instead of abruptly finding a zero density of states below a certain energy at the superconducting transition temperature there was only a partial depression of excitations appearing at a much higher temperature  $T^*$ . This region in the phase diagram has been called the *pseudogap phase* and there is evidence for its presence in all cuprate superconductor families [5, 9]. Within the band-theory approximation, a *pseudogap* occurs when some regions of the Fermi surface become gapped while other parts remain conductive. With increased doping the gapped portion decreases and the compounds become more metallic. However, there is evidence that the pseudogap develops smoothly into the superconducting gap and that there are already preformed charge pairs albeit without long range order [8]. The pseudogap seems a fundamental property of underdoped copper oxides however, although its relationship to superconductivity still remains unclear, it seems that both phases are intimately related [10].

In addition to these peculiarities, cuprate superconductors are intrinsically inhomogeneous systems. For example in  $\text{La}_{1.85}\text{Sr}_{0.15}\text{CuO}_4$  and  $\text{La}_2\text{CuO}_{4.1}$ , the dopant atoms, necessary for superconductivity, do not reside at the crystal symmetric sites making these compounds structurally inhomogeneous [11]. In  $\text{YBa}_2\text{Cu}_3\text{O}_{7-\delta}$  (YBCO) the dopant atoms reside in crystal symmetric positions but the departure from stoichiometry produces compositional disorder [12, 13] making YBCO also an inhomogeneous system. Furthermore, even though the dopant atoms are at fixed positions, these structural inhomogeneities have a dynamical character [14, 15]. Such a dynamical inhomogeneity is present even in some compounds with perfect crystallographic symmetry like  $\text{HoBa}_2\text{Cu}_4\text{O}_8$  [16]. In addition to the breaking of the crystalline translational symmetry, the pseudogap phase exhibits other broken symmetries. The crystalline rotational symmetry is broken locally in  $\text{La}_{1.85}\text{Sr}_{0.15}\text{CuO}_4$  with alternating regions of tetragonal and orthorhombic symmetry [15] according to X-ray absorption spectroscopy. Time-reversal symmetry breaking was found using angular resolved photoemission spectroscopy with circularly polarized photons in  $\text{Bi}_2\text{Sr}_2\text{CaCu}_2\text{O}_{8+\delta}$  [17]. The clues provided by these broken symmetries should yield an understanding of the ground state in this pseudogap phase, its elementary excitations and the appearance of superconductivity at temperatures below the onset of the pseudogap. The existence of these dynamical inhomogeneities suggests that a complete theory of superconductivity is unreachble assuming a perfect crystal structure without consideration for local real-space variations.

Another important aspect to take into consideration is the role of electron-lattice interaction in cuprate superconductors. One strong motivation for Bednorz and Müller to search for superconductivity in  $\text{Ba}_x\text{La}_{5-x}\text{Cu}_5\text{O}_{5(3-y)}$  was the possibility of strong electron-phonon interactions in oxides due to polaron<sup>2</sup> formation [1]. Later X-ray absorption experiments found a large oxygen-isotope effect on the pseudogap onset temperature  $T^*$  which is sign reversed in respect to the isotope effect on  $T_c$ . It was also found that there were local deviations on the Cu-O bond lengths appearing at  $T^*$ . This evidence points to the significance of electron-lattice interactions in the pseudogap phase. In particular the local deviations on the Cu-O bond lengths has been interpreted in terms of polaron formation [18]. The formation of polaronic states is a nonadiabatic phenomenon which breaks the Born-Oppenheimer approximation [19]. Thus, for a complete description of cuprate superconductors, it is impossible to separate the ionic and the electronic motions.

The Bardeen-Cooper-Schrieffer (BCS) theory of superconductivity [20] was developed for and successfully applied to metals within the Fermi-liquid approximation, as such, it seems to lack an appropriate foundation to describe high-temperature superconductivity in copper oxides [21]. The strong electron-electron correlations prevent accurate band structure calculations assuming independent quasiparticles. Furthermore the presence of polaronic objects and the observation of lattice and electronic inhomogeneities point to the inadequacy of the Born-Oppenheimer approximation and the reciprocal space formalism. Such approximations may still remain useful in understanding some aspects of cuprate oxide superconductors but it is clear that there are important features that they are unable to explain.

One approach to explore the electron-lattice dynamics in an inhomogeneous system away from the Born-Oppenheimer (adiabatic) approximation is through model hamiltonians in real space describing both, charge and atomic, degrees of freedom with an appropriate interaction between them. Unfortunately the computationally resources required to deal with such hamiltonians rapidly increase with each degree of freedom introduced thus making unfeasible to explore large systems with many variables. As such, we are forced to focus on small subsystems in the copper oxide superconductors. Since there is strong evidence for polaronic behaviour in the O(4)-Cu(1)-O(4) cluster [18, 22] in the YBCO superconductor it seems essential to correctly describe this subsystem using a non-adiabatic hamiltonian in real space. Furthermore, some models have considered the interaction between fermionic *pairs* and bipolaronic bosonic objects [23, 24, 25, 26] explaining several properties of the normal state in the pseudogap region. The bipolaronic objects could arise from the O(4)-Cu(1)-O(4)

---

<sup>2</sup>A *polaron* is an elementary excitation formed by the correlated movement between a charge and a distortion in the ionic lattice.

cluster and couple to fermionic carriers on the  $\text{CuO}_2$  planes thus raising the importance of correctly describing this subsystem. A particular model hamiltonian has been used to successfully describe the local inhomogeneities and optical signatures in this cluster as a consequence of polaron formation [18, 22, 27, 28, 29, 30, 31, 32]. Although there is a considerable amount of work on this model hamiltonian, the effect of the polaron formation on the *electronic*<sup>3</sup> excitations of the model has not been thoroughly explored. In this thesis we describe in detail this model hamiltonian and many of its lowest excitations including the electronic excitations. It remains as future work to extend this model to include the coupling of the polaronic objects in the  $\text{O}(4)\text{-Cu}(1)\text{-O}(4)$  cluster to superconducting fermionic pairs, although we propose such a model hamiltonian in the conclusions (section 6.2).

The remainder of this introductory chapter is devoted to reviewing some of the experimental results pointing to the importance of considering the charge-lattice coupling as well as the lattice and electronic inhomogeneities in the description of superconductivity. We start, in section 1.2 with an overview of the dynamic local lattice and electronic distortions in cuprate superconductors as observed by several experimental techniques. In sections 1.3 and 1.4 we present some experimental anomalies specific heat and electric resistivity respectively that point to the appearance of a pseudogap and the inapplicability of Fermi-liquid theory. Finally we discuss some of the experimental results in isotopic effects in section 1.5 giving evidence of polaronic effects and the need to correctly describe correlated charge-lattice excitations away from the Born-Oppenheimer approximation.

## 1.2 Dynamic local lattice and electronic inhomogeneities

All cuprate high- $T_c$  superconductors consist of a given number  $n$  of  $\text{CuO}_2$  planes separated by *charge reservoirs*. Some materials, such as  $\text{La}_{2-x}\text{Sr}_x\text{CuO}_4$  and  $\text{Nd}_{2-x}\text{Sr}_x\text{CuO}_4$ , have one  $\text{CuO}_2$  plane per unit cell. Other compounds like  $\text{Bi}_2\text{Sr}_2\text{Ca}_{n-1}\text{Cu}_n\text{O}_{2n+4+x}$  have been synthesized with  $n = 1, 2$  and 3  $\text{CuO}_2$  planes [10]. In this thesis we give particular attention to  $\text{YBa}_2\text{Cu}_3\text{O}_{7-\delta}$  (YBCO) which has two  $\text{CuO}_2$  layers and is one of the most commonly studied compounds.

---

<sup>3</sup>The departure from the Born-Oppenheimer approximation means that the excitations in the model can not be identified as having either a lattice or electronic origin but are always in a *mixed* state of both. Thus, when we refer to an *electronic* excitation we mean an excitation that in the absence of electron-lattice coupling would correspond to the electronic degrees of freedom in the model.

The crystal structure of  $\text{YBa}_2\text{Cu}_3\text{O}_6$  ( $\delta = 1$ ) is tetragonal ( $P4/mmm$  space group) whereas  $\text{YBa}_2\text{Cu}_3\text{O}_7$  ( $\delta = 0$ ) is orthorhombic ( $Pmmm$  space group). The oxygen atoms in YBCO occupy four inequivalent positions and are usually labelled as follows: O(1) is in the Cu-O *chains*, O(2), O(3) are in the  $\text{CuO}_2$  *planes*, and O(4) is the *apical* oxygen (see Figure 1.2). Each oxygen contributes in a different way to the several properties of the material. The sites O(2), O(3), and O(4) are always filled whereas, depending on the value of  $\delta$ , the population of the O(1) sites varies. The  $\delta$  value depends on the growing and treatment conditions specially on the thermal annealing at different atmospheres or vacuum [33]. The two copper atoms in the unit cell also occupy two inequivalent positions. The labels Cu(1) and Cu(2) are usually assigned to copper atoms in the chains and  $\text{CuO}_2$  planes respectively. It is commonly accepted that the Cu(1)-O(1) chains serve as reservoirs for excess holes [34]. At low  $\delta$  the holes are localized at the chains and do not contribute to the conductivity at low temperatures however, at larger  $\delta$ , a hole transfer occurs to the Cu(2)-O(2), O(3) planes and the samples become superconducting [35].

Crystal structure in cuprates was determined first by diffraction methods without any sign of significant distortions associated with the in-plane nor with the apical oxygen atoms [36, 37]. One of the first observations of a local lattice distortion in cuprates was made using Cu K-edge extended X-ray absorption fine structure (EXAFS) measurements. It showed a two distances for the Cu(1)-O(4) bond length in  $\text{YBa}_2\text{Cu}_3\text{O}_7$  at temperatures above the superconducting transition temperature,  $T_c$ , with a difference in length close to  $0.13 \text{ \AA}$  [38, 39]. Since the average bond lengths in diffraction have a significantly higher precision ( $\sim 0.001 \text{ \AA}$  [40]) than local probes like EXAFS [41], these reports were controversial [42]. To resolve the controversy, it was noticed that the time scale in EXAFS measurements is such that dynamical distortions can be measured but, depending on the size of the distortion, elastic techniques like X-ray or neutron diffraction are unable to detect them [27]. For example, it was shown that the two-site O(4) distribution in  $\text{Tl}_2\text{Ba}_2\text{CaCu}_2\text{O}_8$  could be only detected in a pair distribution function obtained from neutron inelastic scattering but not with that obtained from neutron diffraction [43]. Consequently, it is important to take into account both the spatial resolution and time resolution of the techniques used to study the actual atomic structure of these materials [14]. The explanation of the discrepancies between these results with diffraction and optical spectroscopical results lead to the interpretation of this two-sites Cu(1)-O(4) distribution as a dynamical distortion of polaronic origin [18].

In  $\text{YBa}_2\text{Cu}_3\text{O}_7$  the EXAFS analysis using polarized X-rays on magnetically oriented powders showed two different Cu(1)-O(4) distances differing by  $\sim 0.10 - 0.13 \text{ \AA}$  that changed into a single site distribution in the vicinity of the superconducting

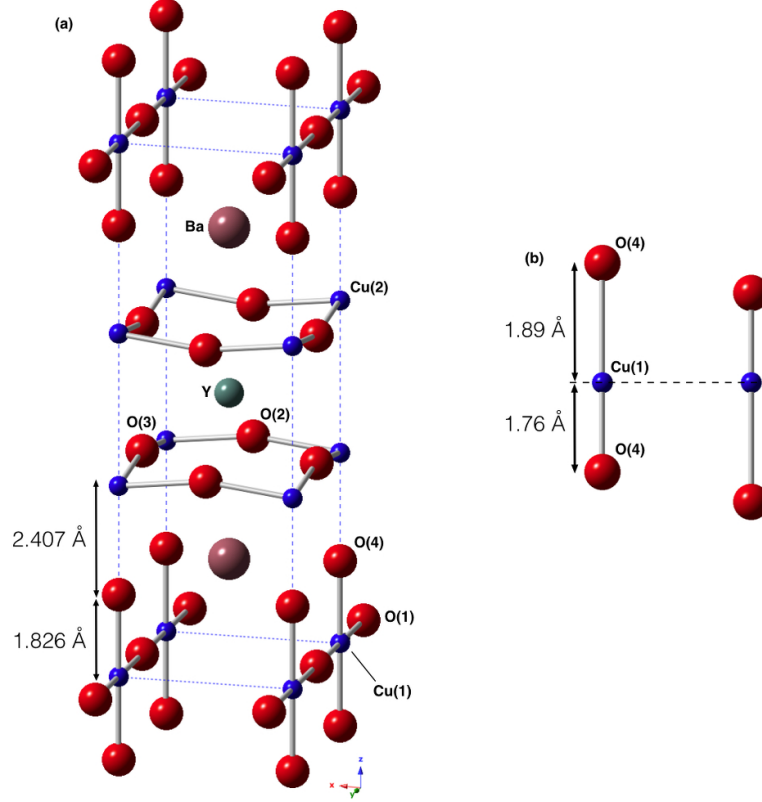


Figure 1.2: (a) Crystal structure of  $\text{YBa}_2\text{Cu}_3\text{O}_7$ . The dashed line denotes de unit cell. (b) The two possible configurations in the O(4)-Cu(1)-O(4) cluster due to the split O-Cu bond distances (not to scale).

transition temperature [39, 44]. This result was also received with skepticism based on earlier diffraction [45, 42, 46] and optical spectroscopy [47] results. However, independent EXAFS measurements in other oriented samples [48] and single crystals [49] also showed a two-site distribution in  $\text{YBa}_2\text{Cu}_3\text{O}_{6.7}$ ,  $\text{YBa}_2\text{Cu}_3\text{O}_{6.5}$  and Co doped  $\text{YBa}_2\text{Cu}_{2.8}\text{Co}_{0.2}\text{O}_{7+\delta}$  [50].

Similar two site distributions obtained from EXAFS spectra were found for the Cu(2)-O(4) distribution in  $\text{Bi}_2\text{Sr}_2\text{CaCu}_2\text{O}_8$  [51] and in  $\text{TlBa}_2\text{Ca}_3\text{Cu}_4\text{O}_{11}$  [52] starting at temperatures above  $T_c$ . In these compounds (and other cuprates) the average Cu(2)-O(4) bond length lies between  $2.49$  and  $2.73 \text{ \AA}$ , which is much longer than the Cu(1)-O(4) bond length in  $\text{YBa}_2\text{Cu}_3\text{O}_7$  ( $\sim 1.87 \text{ \AA}$ ). This fact makes more difficult the identification of details about the O(4) distribution due to the stronger mixing of the Cu(2)-O(4) EXAFS signal with those of other atoms and the increased zero

point motion of the O(4) atom due to weaker Cu(2)-O(4) bond compared with the Cu(1)-O(4) bond. For this reason in most EXAFS studies addressing the O(4) motion a gaussian single site broadened distribution has been used, reporting only changes in the width of the distribution as a function of temperature [53, 54, 55].

In plane Cu(2)-O local lattice distortions were identified in  $\text{La}_{1.85}\text{Sr}_{0.15}\text{CuO}_4$  appearing below 100 K [15, 54], in  $\text{TlBa}_2\text{CuO}_6$  below 120 K [56] and in  $\text{La}_2\text{CuO}_{4.1}$  below 150 K [57, 58]. In this case the observation of such distortions in  $\text{YBa}_2\text{Cu}_3\text{O}_7$  and related compounds becomes more difficult due the similarity in Cu-O bond lengths in the  $\text{CuO}_2$  planes and chains, whose contributions are mixed in the EXAFS signal [56, 44].

As of now only in  $\text{La}_{1.85}\text{Sr}_{0.15}\text{CuO}_4$  has been possible to identify local lattice distortions involving both in plane oxygen and apical oxygen atoms [15]. We also stress that from all these EXAFS experiments it is only possible to probe with enough detail the nearest neighbor environment around the Cu atoms, thus the spatial extension of the distortions cannot be determined solely from these measurements. Additional structural information [59] is needed to formulate models about the extension of the distortions as discussed in Ref. [15]. Pair distribution function analysis of diffraction, X-ray and neutron inelastic scattering can additionally provide information about the intermediate range (up to 10-15 Å) atomic structure, complementary to the information obtained from EXAFS [60]. Pair distribution function results in  $\text{La}_{1-x}\text{Sr}_x\text{CuO}_4$  [61, 62] indicate that the atomic structure in this material is a combination of nanoscale regions with different local Cu-O environments, in agreement with the model proposed in Ref. [15]. A homogeneous structure only appears when dopant concentrations are above  $x = 0.25$ . In this region the electronic behavior can be described in terms of free fermion quasiparticles.

Although an inhomogeneous electronic ground state does not necessarily follow from structural inhomogeneities, such as the ones discussed in the previous section, for some regions of the phase diagram such state is realized. Early EXAFS analysis in  $\text{La}_{1.85}\text{Sr}_{0.15}\text{CuO}_4$  and X-ray diffraction in  $\text{Bi}_2\text{Sr}_2\text{CaCu}_2\text{O}_{8+y}$  showed two orders of the  $\text{CuO}_6$  octahedra below 100K assigned to two types of *stripes* with different order, one of them with a large tilting and elongation of the in-plane Cu-O distances. This significant distortion was taken as an indicative that the electronic structure in both kind of stripes is different [15, 59]. Since then it has been possible to detect the existence of stripe-ordered phases in  $\text{La}_2\text{CuO}_{4+\delta}$ ,  $\text{La}_{1.6-x}\text{Nd}_{0.4}\text{Sr}_x\text{CuO}_4$ ,  $\text{La}_{2-x}\text{Ba}_x\text{CuO}_4$ ,  $\text{La}_{2-x}\text{Sr}_x\text{CuO}_4$  [63],  $\text{Bi}_2\text{Sr}_2\text{CaCu}_2\text{O}_{8+\delta}$  [64] and  $\text{YBa}_2\text{Cu}_3\text{O}_{7-\delta}$  [65, 66]. Spatial variations in the density of states (stripes) have also been measured using scanning tunneling microscopy (STM) [67] and angle-resolve photoemission spectroscopy (ARPES) [68].



## 1.3 Specific heat

Specific heat ( $C$ ) measurements in bulk superconductors can provide useful information about the superconducting and normal states. Important quantities for the conventional theory of superconductivity, such as the density of electronic states at the Fermi energy and the Debye characteristic temperature, can be obtained from specific heat measurements below  $T_c$  in a magnetic field exceeding the upper critical field ( $H_{c2}$ ), that is, with superconductivity suppressed. The density of states at the Fermi energy can be obtained from the linear term ( $\gamma T$ ) of the specific heat while the Debye characteristic temperature from the  $T^3$  term. The specific heat comprised of the odd polynomial terms is the *lattice* part ( $C_l$ ) and gives some information about phonon dispersion. The electronic specific heat in the superconducting state ( $C_{es}$ ) can be obtained by subtracting  $C_l$  from zero-field measurements. The discontinuity in  $C$  at  $T_c$  and  $C_{es}$  are related to the magnitude of the electron-phonon coupling in conventional BCS superconductors. Thus the temperature dependence of  $C_{es}$  might show evidence of certain different mechanisms of superconductivity, although some non-BCS mechanisms could give the usual BCS result.

Unfortunately, for cuprate superconductors there are several problems hindering the analysis of specific heat experiments. One of them is that  $T_c$  typically occurs in temperature regions in which  $C_l$  is about a hundred times larger than other contributions and has a complicated temperature dependence. Another problem arises from the fact that the upper critical fields  $H_{c2}$  are usually too large to suppress superconductivity and obtain normal-state information except at temperatures close to  $T_c$ . Also, there are magnetic impurities that complicate the interpretation at low temperatures [69].

Nevertheless, electronic specific heat was successfully measured using a differential technique comparing a superconducting sample with a very similar non-superconducting sample. Although some corrections have to be made due to the change in phonon spectrum between samples, the electronic specific heat can be largely determined by this method [70, 71, 72]. An ensuing investigation of the electronic specific heat of  $\text{Y}_{0.8}\text{Ca}_{0.2}\text{Ba}_2\text{Cu}_3\text{O}_{7-\delta}$  as a function of oxygen doping ( $0.04 \leq \delta \leq 0.89$ ) showed very different behaviours for the electronic specific heat coefficient  $\gamma(T) = C/T$  in the underdoped ( $\delta > 0.32$ ) and overdoped ( $\delta < 0.32$ ) samples [73].

In the overdoped samples, (see FIG 2 (a) from [73]),  $\gamma(T)$  is temperature independent if the sample is in its normal state. Since for a Fermi liquid the specific heat rises linearly with the temperature (i.e.  $\gamma(T)$  is constant) this suggests that the overdoped sample is similar to a normal metal. At  $T_c$  there is a specific heat jump which is larger than what is expected for a BCS model assuming a weak coupling

suggesting that superconductivity in copper oxides is driven by strong couplings.

In the underdoped samples there is a plateau where  $T_c$  varies slowly but there is a sudden decrease in the height of the specific heat jump at  $T_c$ . In these underdoped samples there is a depression of  $\gamma(T)$  in the normal state which is interpreted as a consequence of a pseudogap. This depression starts at higher temperatures when more oxygen is removed. There has been similar evidence of a pseudogap in the normal state for some more hole-doped cuprates [74].

## 1.4 Electric resistivity

In conventional (Fermi-liquid) metals the electric resistivity,  $\rho(T)$ , at low temperatures is a linear function of temperature intercepting the temperature axis at some point and saturating at high temperatures. In contrast, the electric resistivity in optimally doped copper oxide superconductors was found to be a linear function of temperatures for a wide range  $\sim 10 - 1000$  K and extrapolates to zero resistivity at zero degrees [5, 9]. In the underdoped materials there is a break in the slope of this linear behaviour at a temperature near the pseudogap onset temperature  $T^*$  as observed by nuclear magnetic resonance [75].

The doping dependence of the electric resistivity in the ab-plane,  $\rho_{ab}(T)$ , which is parallel to the  $\text{CuO}_2$  planes, is qualitatively different in the underdoped and overdoped compounds. For the underdoped samples, at low temperatures  $\rho_{ab}(T)$  shows *semiconducting* behaviour with the resistivity decreasing with temperature down to a minimum before increasing again superlinearly up to  $T^*$  where a break in slope makes  $\rho_{ab}$  approximately linear [5]. In the overdoped samples the resistivity shows an approximately linear dependence with  $T$  [21] similar to the Fermi-liquid behaviour, however this linear behaviour extends to much higher temperatures than expected and there are many other properties that do not follow the expected Fermi-liquid behaviour [8].

These measurements show both, the inapplicability of Fermi-liquid theory to the copper oxides and the presence of a pseudogap in the underdoped samples.

## 1.5 Isotopic effects

The effect of isotopic substitutions were important in the understanding and validation of BCS superconductivity. This effect manifests itself as a change in the superconducting transition temperature ( $T_c$ ) with the ionic mass ( $M$ ) in the form  $T_c \propto M^{-\alpha}$  where  $\alpha$  is called the *isotope coefficient*. In the simplest case of a monoatomic lattice

in a BCS superconductor it takes the value  $\alpha = 0.5$ . The observation of this isotope effect [76, 77] was evidence of the crucial role played by the electron-lattice interaction in the formation of Cooper pairs. In complex materials, such as the cuprate superconductors, there are many factors that can affect the value of the isotope coefficient, such as the presence of several ions, lattice anharmonicity, inhomogeneities and polaronic effects. All these factors complicate the interpretation of the isotope effects observed in cuprates.

The isotope effect and its temperature dependence has been extensively studied in copper oxides. Its behaviour is very different from what can be expected for a simple BCS superconductor. In particular, YBCO allows a site-selective substitution  $^{16}\text{O} \rightarrow ^{18}\text{O}$  enabling a precise study of the isotopic effect for each different oxygen site [78, 79]. At optimal doping  $\alpha$  was observed to be relatively small [80], however it grows significantly by reducing the doping level [81]. Making site-specific substitutions and measuring the changes in the phonon frequencies allowed a differentiation of the contributions of the different ions. It was found that the (small) isotope effect on  $T_c$  mainly comes from in-plane oxygens with little contribution from the apical oxygen [82, 83]. Since the superconducting charge carriers reside in the  $\text{CuO}_2$  planes, this suggests a fundamental role of the lattice dynamics in the superconducting state. Also, it was found that the *harmonic* approximation accounts well for the O(2)/O(3) vibrations but it fails for O(4) [82].

Another observable quantity that shows an isotope effect is the London penetration depth  $\lambda_L$ . At optimum doping, in contrast to what is observed for  $T_c$ , the isotope effect is rather large in  $\lambda_L$  and it similarly increases with a decrease in doping [84, 85, 86]. It should be noted that in a conventional BCS superconductor the isotope effect on  $\lambda_L$  is zero. Similarly for the two-gap superconductor  $\text{MgB}_2$ , in which superconductivity is mediated by electron-phonon interactions, there is no isotope effect in  $\lambda_L$  [87]. This isotope effect in cuprate oxides further suggests that the ionic lattice and the electron-lattice interaction are fundamentally involved in the appearance of superconductivity in these compounds [88]. It even has been argued that from the isotope effects in the London penetration depth follows that the carriers are polaronic objects with an oxygen-isotope dependent in-plane effective supercarrier mass [84, 85, 86].

Another isotope effect was found on the pseudogap onset temperature  $T^*$  using two different experimental techniques, EXAFS and inelastic neutron scattering, in the  $\text{La}_{1-x}\text{Sr}_x\text{CuO}_4$  and  $\text{HoBa}_2\text{Cu}_4\text{O}_8$  compounds [89, 16]. These experiments show a very large isotope effect that is sign-reversed with respect to the effect on  $T_c$ .

Lastly, there is a report of a large isotope effect in the electronic structure on optimally doped  $\text{Bi}_2\text{Sr}_2\text{CaCu}_2\text{O}_{8+\delta}$  samples measured by ARPES. This was interpreted in

terms of a significant pairing between electrons and the ionic lattice with the magnitude of the effect correlated with the pair binding energy [90]. However, a later study failed to find such large isotope effect [91] in the same compound. To our knowledge this controversy still remains unresolved. In the present work, in section 5.3, we find an isotope effect in the electronic structure of  $\text{YBa}_2\text{Cu}_3\text{O}_{7-\delta}$  under an oxygen isotope substitution (to be published). However we are still lacking a clear interpretation of our results in terms its measurable effects on ARPES measurements preventing us to draw a significant conclusion at the moment.

Additionally, it should be noted that isotopic shifts have been used to identify particular excitations in infrared and Raman spectra as phononic in origin (v.g. [92]) however, as we will discuss in section 4.3, in the case of the apical oxygen, due to polaronic effects, a *phononic* excitation could have an isotope effect very close to zero.

## Chapter 2

# Peierls-Hubbard model

As mentioned in section 1.1, treatments based in the adiabatic and antiadiabatic approximations are unable to describe properly the correlated charge-ion motion in cuprate's Cu-O bonds. An alternative to overcome this limitation is an exact treatment of a reduced system. In this thesis we focus on the O(4)-Cu(1)-O(4) cluster in  $\text{YBa}_2\text{Cu}_3\text{O}_7$ . We approximate this local environment as a three site cluster with two holes. Such approximation is justified as the Cu(1)-O(4) bond length (1.83 Å) is far shorter than the Cu(2)-O(4) bond length ( $\sim 2.41$  Å) (see figure 1.2), making charge transfer outside the cluster a much slower process than the charge dynamics inside the cluster. Although we cannot directly identify the three site cluster proposed in this model with a particular structure of the CuO plane, the general approach of charge transfer between hole rich regions and hole poor regions in the plane coupled to the lattice degrees of freedom is still valid, hence the general conclusions we draw from this model are applicable to describe the structure of the CuO plane.

This thesis is based in a thorough analysis of that model hamiltonian so we devote this chapter to a detailed description of its components. In section 2.1 we describe the hamitlonian and the basis used. Section 2.4 reviews a method of incorporating isotopic substitutions in this model and defines *isotopic shifts* in this context. In section 2.2 we discuss a method of calculating real-space lattice distortions. Next, in section 2.3, we describe a projection into definite charge occupation states. Section 2.6 reviews some literature suggesting possible choices of parameters and lists the parameters used in this work. We review in section 4.1 a method for identifying and classifying the different excitations in this model. Finally, appendix A gives some computational details about our calculations.

## 2.1 Hamiltonian and basis set

To describe two holes in the O(4)-Cu(1)-O(4) cluster with an charge-ion (phonon) correlated movement we use a hamiltonian consisting of three parts:

$$H = H_{el} + H_{ph} + H_{el-ph} \quad (2.1)$$

corresponding to the electronic contribution, the phonon energies and the electron-phonon (lattice) coupling, respectively [22]. The electron-phonon coupling term deviates this model from the Born-Oppenheimer (adiabatic) approximation and prevents the separation of hamiltonian eigenstates,  $\Psi$ , as products of purely electronic and phononic parts,  $\Psi = \psi_{el}\psi_{ph}$ , unless  $H_{el-ph} = 0$ . Nonetheless, as it will be discussed in section 4.1, even for coupling values greater than zero the hamiltonian eigenstates can be interpreted as mainly *electronic* or *phononic* in nature.

The electronic part is modeled as a single band Hubbard model for three sites with two holes in it. We only consider the two holes as having opposite spin because the energies of states with two charges with the same spin are much greater. Explicitly,  $H_{el}$  is written as

$$H_{el} = \sum_{\sigma, i=1}^3 E_i n_{i\sigma} + U \sum_{i=1}^3 n_{i\downarrow} n_{i\uparrow} + t \sum_{\sigma} \left( c_{1\sigma}^\dagger c_{2\sigma} + c_{2\sigma}^\dagger c_{3\sigma} + H.c. \right) \quad (2.2)$$

where we denoted  $n_{i\sigma} = c_{i\sigma}^\dagger c_{i\sigma}$  as the hole-number operator with  $c_{i\sigma}^\dagger$  creating a hole with spin  $\sigma = \uparrow, \downarrow$  and  $c_{i\sigma}$  destroying it; the site index  $i = 1, 2, 3$  indicates the two oxygen sites [O(4)] when  $i = 1, 3$  and the only copper site [Cu(1)] when  $i = 2$ . The site energies are parametrized with  $E_1 = E_3 = -E_2 \equiv E_0$ .<sup>1</sup>  $U$  is the on-site Coulomb interaction and  $t$  is the hopping energy between two adjacent sites.

For the lattice part of the Hamiltonian,  $H_{ph}$ , we consider both symmetric (Raman) and antisymmetric (infrared) modes described by boson operators  $b_R$  and  $b_{ir}$  and bare frequencies  $\omega_R$  and  $\omega_{ir}$  respectively,<sup>2</sup>

$$H_{ph} = \hbar\omega_{ir} \left( b_{ir}^\dagger b_{ir} + \frac{1}{2} \right) + \hbar\omega_R \left( b_R^\dagger b_R + \frac{1}{2} \right) \quad (2.3)$$

<sup>1</sup>In [27] the authors consider an example of *disorder* in this system by letting  $E_1 \neq E_3$ .

<sup>2</sup>Unlike previous publications, here we include the *zero-point energy* for both phonon modes. For most cases this is not needed since the excitation's energies are calculated relative to the ground state but, in chapter 3 we study the ground state energy itself where this contribution is important.

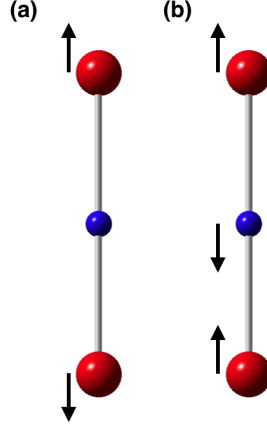


Figure 2.1: Schematic showing the (a) symmetric (Raman) and (b) antisymmetric (infrared) vibrational modes for the  $\text{CuO}_2$  cluster.

The electron-lattice coupling term,  $H_{el-ph}$  is introduced through the change in interatomic distances generated by Coulomb repulsion between different sites coupled with the Raman and infrared phonon modes,

$$H_{el-ph} = \tilde{\lambda}_{ir} u_{ir} (n_3 - n_1) + \tilde{\lambda}_R u_R (n_1 + n_3 - s_0) \quad (2.4)$$

Here  $u_{ir}$  and  $u_R$  are the *phonon coordinates* for the infrared and Raman modes respectively, they are related to the atomic coordinates  $x_i = 1, 2, 3$  by

$$u_R \equiv \left( \frac{\hbar}{2m_R \omega_R} \right)^{1/2} (b_R^\dagger + b_R) = \frac{x_3 - x_1}{\sqrt{2}} \quad (2.5)$$

$$u_{ir} \equiv \left( \frac{\hbar}{2m_{ir} \omega_{ir}} \right)^{1/2} (b_{ir}^\dagger + b_{ir}) = \frac{x_1 + x_3 - (2m_O/m_{Cu})x_2}{(2 + 4m_O/m_{Cu})^{1/2}} \quad (2.6)$$

with  $m_{ir}$  and  $m_R$  being the reduced mass for each mode (see (2.41, 2.42) below),  $x_i = 2$  the position of the central copper atom and  $x_i = 1, 3$  the positions of the oxygen atoms. The constant  $s_0$  is introduced to avoid artificial shrinking of the cluster<sup>3</sup>. For consistency with other works [18, 28, 29, 30] we fix  $s_0 = 4/3$ . Using the

<sup>3</sup>This term is written slightly different in some publications, for example in [18],  $H_{el-ph}$  is proportional to  $n_1 - n_2 + n_3$ . However both versions can be related noticing that  $3(n_1 + n_3 - 4/3) = n_1 - 2n_2 + n_3$ .

definitions (2.5, 2.6) we can rewrite (2.4) as

$$H_{el-ph} = \lambda_{ir}(b_{ir} + b_{ir}^\dagger)(n_3 - n_1) + \lambda_R(b_R + b_R^\dagger)(n_1 + n_3 - s_0) \quad (2.7)$$

With

$$\lambda_R = \tilde{\lambda}_R(\hbar/2m_R\omega_R)^{1/2}, \quad \lambda_{ir} = \tilde{\lambda}_{ir}(\hbar/2m_{ir}\omega_{ir})^{1/2} \quad (2.8)$$

From the definition of  $H_{el-ph}$  we can observe that the electrons will be coupled to the infrared (antisymmetric) mode only when one charge is located at the copper site and the other in an oxygen. However, there will be electron-lattice coupling with the Raman (symmetric) mode in all cases.

One simple basis set for this system can be denoted as  $\{|e_1, e_2, ir, R\rangle : e_1, e_2 = 1, 2, 3; ir, R = 1, 2, \dots\}$  with  $e_k$  being the position of the  $k$ -th hole,  $ir$  the number of *infrared* phonons and  $R$  the number of *Raman* phonons. This basis is infinite dimensional however, as discussed in appendix A, for the lower energy excitations the eigenvalues and eigenvectors are well described using a basis with only a few phononic excitations.

## 2.2 Lattice distortions

With the atomic coordinates  $x_i$  as defined before ( $i = 1, 3$  for the oxygens and  $i = 2$  for the copper) the distance difference  $d$  between one O-Cu bond and the other is

$$d = (x_3 - x_2) - (x_2 - x_1) = x_1 + x_3 - 2x_2 \quad (2.9)$$

The  $x_i$  coordinates are varying at all times but taking an instant in which  $x_2 = 0$  we can simplify (2.9) to

$$d = x_1 + x_3 \quad (2.10)$$

Which can be related to the phonon coordinate  $u_{ir}$  by using (2.6) with  $x_2 = 0$ ,

$$u_{ir} = \frac{x_1 + x_3}{(2 + 4m_O/m_{Cu})^{1/2}} \quad (2.11)$$

Substitution (2.10) into (2.11) and solving for  $d$  gives

$$d = \sqrt{2} \left( 1 + 2 \frac{m_O}{m_{Cu}} \right)^{1/2} u_{ir} \quad (2.12)$$

which is a relationship between the phonon coordinates, that can be calculated from the model's eigenfunctions, and the observable lattice distortion. Equation (2.12)



allows a connection between this model hamiltonian and a specific experimental observation. It is this relationship that helps fixing the free coupling parameters  $\lambda_{ir}$  and  $\lambda_R$  in this model.

In the remainder of this section we show how to find the most probable  $u_{ir}$  value for a given state in the model hamiltonian (2.1). To do this we first take as an example a simple quantum harmonic oscillator

$$H = \hbar\omega \left( a^\dagger a + \frac{1}{2} \right) \quad (2.13)$$

with mass  $m$  and frequency  $\omega$ . The creation ( $a^\dagger$ ) and annihilation ( $a$ ) operators are related to the real-space position coordinate  $u$  as

$$u = \sqrt{\frac{\hbar}{2m\omega}} (a + a^\dagger) \quad (2.14)$$

An energy eigenfunction,  $|n\rangle$  where  $n$  labels the *number of phonons*, has a projection into the real space coordinate  $u$  given in terms of a Hermite polynomial  $H_n(u)$  of degree  $n$  in the following way,

$$\langle u|n\rangle \equiv \psi_n(u) = \frac{1}{\sqrt{2^n n!}} \left( \frac{m\omega}{\pi\hbar} \right)^{1/4} \exp\left(-\frac{m\omega u^2}{2\hbar}\right) H_n\left(\sqrt{\frac{m\omega}{\hbar}} u\right) \quad (2.15)$$

An arbitrary wavefunction  $|\psi\rangle$  can be expanded in terms of the energy eigenfunctions as  $|\psi\rangle = \sum_n \langle n|\psi\rangle |n\rangle$  and projected in real space:  $\langle u|\psi\rangle = \sum_n \langle n|\psi\rangle \langle u|n\rangle$  with  $\langle u|n\rangle$  given by (2.15).

Now, returning to the model hamiltonian (2.1), as discussed in section 2.1, a possible basis set is given by the functions  $|e_1, e_2, ir, R\rangle$  with  $e_i$  the position of the  $i$ -th electron and  $ir, R$  the number of infrared and Raman phonons respectively. Thus an arbitrary wavefunction in this system,  $|\psi\rangle$ , can be expanded in this basis as

$$|\psi\rangle = \sum_{e_1, e_2, ir, R} \langle e_1, e_2, ir, R|\psi\rangle |e_1, e_2, ir, R\rangle \quad (2.16)$$

and we can make the partial projection into the phonon coordinates  $(u_{ir}, u_R)$  as defined by (2.5, 2.6) in the following way

$$\langle u_{ir}, u_R|\psi\rangle = \sum_{e_1, e_2, ir, R} \langle e_1, e_2, ir, R|\psi\rangle \langle u_{ir}, u_R|ir, R\rangle |e_1, e_2\rangle \quad (2.17)$$

where we have denoted  $\langle u_{ir}, u_R | e_1, e_2, ir, R \rangle$  as  $\langle u_{ir}, u_R | ir, R \rangle | e_1, e_2 \rangle$ . The term  $\langle u_{ir}, u_R | ir, R \rangle$  is similar to (2.15) but considering both phonon modes:

$$\langle u_{ir}, u_R | ir, R \rangle = \frac{(m_{ir} m_R)^{1/4}}{\sqrt{2^{(ir+R)} ir! R! \pi \hbar}} \exp \left( -\frac{\tilde{u}_{ir}^2 + \tilde{u}_R^2}{2} \right) H_{ir}(\tilde{u}_{ir}) H_R(\tilde{u}_R) \quad (2.18)$$

where we have defined the normalized coordinates,

$$\tilde{u}_j \equiv \sqrt{\frac{m_j \omega_j}{\hbar}} u_j \quad (2.19)$$

for  $j = ir, R$ . The reduced mass constants  $m_{ir}, m_R$  are determined later in (2.41, 2.42) from section 2.4.

Since we are interested in finding real-space distortions in the cluster we now use (2.17) to find the probability amplitude of finding a state  $|\psi\rangle$  projected into phonon coordinates  $(u_{ir}, u_R)$  for a given charge occupation  $(e_1, e_2)$ :

$$\begin{aligned} & |\langle e_1, e_2, u_{ir}, u_R | \psi \rangle|^2 \\ &= \left| \sum_{e'_1, e'_2, ir, R} \langle e_1, e_2, ir, R | \psi \rangle \langle u_{ir}, u_R | ir, R \rangle \langle e_1, e_2 | e'_1, e'_2 \rangle \right|^2 \\ &= \left| \sum_{ir, R} \langle e_1, e_2, ir, R | \psi \rangle \langle u_{ir}, u_R | ir, R \rangle \right|^2 \end{aligned} \quad (2.20)$$

The probability amplitude of finding a system in the state  $|\psi\rangle$  with phonon coordinates  $(u_{ir}, u_R)$  irrespective of the electronic configuration is given by the sum over the electronic degrees of freedom on the previous equation,

$$\begin{aligned} |\psi(u_{ir}, u_R)|^2 &\equiv \sum_{e_1, e_2} |\langle e_1, e_2, u_{ir}, u_R | \psi \rangle|^2 \\ &= \sum_{e_1, e_2} \left| \sum_{ir, R} \langle e_1, e_2, ir, R | \psi \rangle \langle u_{ir}, u_R | ir, R \rangle \right|^2 \end{aligned} \quad (2.21)$$

with  $\langle u_{ir}, u_R | ir, R \rangle$  given by (2.18).

To find the most probable cluster distortion  $d$  we can find the value of  $u_{ir}$  that produces a maximum in the projection (2.21) and substitute it in (2.12). This is done in section 3.1 in the next chapter.

## 2.3 Charge localization

Eigenstates of the hamiltonian (2.1), in general, have delocalized charges. To understand charge dynamics for each excitation it is useful to project the eigenstates into the definite charge occupation basis states discussed in section 2.1. The basis set we are using ( $\{|e_1, e_2, ir, R\rangle\}$ ) has sharp values for the hole number operator on each site for a given number of infrared  $ir$  and Raman  $R$  phonons. Thus, to find the probability  $P(e_1, e_2)$  of finding one hole in site  $e_1$  and the other on site  $e_2$ , we need only to sum over the infrared and Raman phonons of the system,

$$P(e_1, e_2) = \sum_{ir, R} |\langle e_1, e_2, ir, R | \psi \rangle|^2 \quad (2.22)$$

From the labeling convention stated in (A.1) we can visualize the nine possible combinations of hole occupancy. Denoting, for example,  $e_1$  as  $\uparrow$  and  $e_2$  as  $\downarrow$  we have the following combinations:

$$\begin{aligned} 1 &= \uparrow\downarrow & - & - \\ 2 &= \uparrow & \downarrow & - \\ 3 &= \uparrow & - & \downarrow \\ 4 &= \downarrow & \uparrow & - \\ 5 &= - & \uparrow\downarrow & - \\ 6 &= - & \uparrow & \downarrow \\ 7 &= \downarrow & - & \uparrow \\ 8 &= - & \downarrow & \uparrow \\ 9 &= - & - & \uparrow\downarrow \end{aligned} \quad (2.23)$$

Since the model hamiltonian (2.1) does not distinguish spin and the cluster is symmetrical, states  $\{1, 9\}$  are equivalent, as well as  $\{2, 4, 6, 8\}$  and  $\{3, 7\}$ .

## 2.4 Isotopic substitutions

The effects of isotopic substitutions in cuprate superconductors have been extensively studied and can reveal fundamental properties of the material (see section 1.5). It is, therefore, of interest to model these effects on the three sites cluster we are studying.

Changing the atomic mass in any of the three atomic sites should change the phonon frequencies ( $\omega_{ir}, \omega_R$ ) in (2.3). To calculate this change in frequencies we continue to model the infrared and Raman vibrational modes in the O(4)-Cu(1)-O(4) cluster as harmonic oscillators. In this section we consider a classical model of three masses ( $m_i$ ,  $i = 1, 2, 3$  with  $i = 1, 3$  for the oxygen and  $i = 2$  for the copper atoms)

attached by springs of constants  $k_1$  and  $k_2$  (see figure 2.2) and find the dependence of the normal vibrational modes on the mass of each atom. In our particular case we are interested in  $m_1 = m_3$  and  $k_1 = k_2$ , but we start from the slightly more general case.

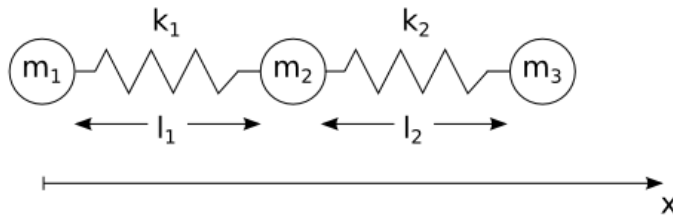


Figure 2.2: Diagram for 3 masses attached with springs representing the nuclei motion.

We will look only at the motion in the longitudinal direction so we attach a reference frame and call, as before,  $x_i$  ( $i = 1, 2, 3$ ) the coordinate describing the position of  $m_i$ . A lagrangian  $L$  for this system is

$$L = T - V \quad (2.24)$$

$$= \frac{1}{2} \sum_{i=1}^3 m_i \dot{x}_i^2 - \frac{1}{2} k_1 (l_1 - (x_2 - x_1))^2 + \frac{1}{2} k_2 (l_2 - (x_3 - x_2))^2 \quad (2.25)$$

It will be more convenient to change the  $x_i$  coordinates to another set reflecting only the displacements from the equilibrium position. That is, we define new coordinates  $\eta_i$  such that  $(x_1, x_2, x_3) = (\eta_1, l_1 + \eta_2, l_1 + l_2 + \eta_3)$ . In this coordinate system the lagrangian looks simpler

$$L = \frac{1}{2} \sum_{i=1}^3 m_i \dot{\eta}_i^2 - \frac{1}{2} k_1 (\eta_1 - \eta_2)^2 + \frac{1}{2} k_2 (\eta_2 - \eta_3)^2 \quad (2.26)$$

The potential energy is a quadratic function of the  $\eta_i$  displacements so we can write it in the general form  $V = \frac{1}{2} \sum_{i,j} V_{ij} \eta_i \eta_j$  where  $V_{ij}$  are the elements of the matrix defined as

$$(V_{ij}) = \begin{pmatrix} k_1 & -k_1 & 0 \\ -k_1 & k_1 + k_2 & -k_2 \\ 0 & -k_2 & k_2 \end{pmatrix} \quad (2.27)$$

The dynamics of the system is determined by the Euler-Lagrange equations,

$$0 = \frac{d}{dt} \frac{\partial L}{\partial \dot{\eta}_s} - \frac{\partial L}{\partial \eta_s} \quad (2.28)$$

$$= m_s \ddot{\eta}_s + \sum_i V_{is} \eta_i \quad (2.29)$$

for  $s = 1, 2, 3$ . We can propose an oscillatory solution of the form  $\eta_i = a_i e^{i\omega t}$ , understanding that only the real part of this equations is physically significant. Substituting this solution into the equations of motion (2.29), after removing the common exponential factor, gives

$$0 = \sum_i V_{is} a_i - \omega^2 m_s a_s \quad (2.30)$$

which can be arranged as a matrix

$$\begin{pmatrix} 0 \\ 0 \\ 0 \end{pmatrix} = (V_{ij}) \begin{pmatrix} a_1 \\ a_2 \\ a_3 \end{pmatrix} - \omega^2 \begin{pmatrix} m_1 & 0 & 0 \\ 0 & m_2 & 0 \\ 0 & 0 & m_3 \end{pmatrix} \begin{pmatrix} a_1 \\ a_2 \\ a_3 \end{pmatrix} \quad (2.31)$$

Substituting the actual values for  $(V_{ij})$ :

$$\begin{pmatrix} 0 \\ 0 \\ 0 \end{pmatrix} = \begin{pmatrix} k_1 - \omega^2 m_1 & -k_1 & 0 \\ -k_1 & k_1 + k_2 - \omega^2 m_2 & -k_2 \\ 0 & -k_2 & k_2 - \omega^2 m_3 \end{pmatrix} \begin{pmatrix} a_1 \\ a_2 \\ a_3 \end{pmatrix} \quad (2.32)$$

In order to have a non-trivial solution we require the determinant of that matrix to be zero

$$0 = (k_1 - \omega^2 m_1)(k_1 + k_2 - \omega^2 m_2)(k_2 - \omega^2 m_3) - k_1^2(k_2 - \omega^2 m_3) - k_2^2(k_1 - \omega^2 m_1) \quad (2.33)$$

which is a third order algebraic equation for  $\omega^2$  with 3 solutions for  $\omega$ . To simplify the calculation we take now into consideration the details of our problem, that is, we consider  $m_1 = m_3 \equiv m_O$ ,  $m_2 \equiv m_{Cu}$  and  $k_1 = k_2 \equiv k$ . With this considerations, (2.33) simplifies to

$$0 = (k - \omega^2 m_O)^2 (2k - \omega^2 m_{Cu}) - 2k^2 (k - \omega^2 m_O) \quad (2.34)$$

$$= (k - \omega^2 m_O) [(k - \omega^2 m_O)(2k - \omega^2 m_{Cu}) - 2k^2] \quad (2.35)$$

from which we can observe one solution

$$\omega^2 = \frac{k}{m_O} \quad (2.36)$$

corresponding to the symmetrical (Raman) vibrational mode, denoted by  $\omega_R$  in 2.3, since it doesn't depend on  $m_{Cu}$ . The other two frequencies are obtained from the remaining factor in 2.34,

$$\begin{aligned} 0 &= (k - \omega^2 m_O)(2k - \omega^2 m_{Cu}) - 2k^2 \\ &= 2k^2 - k\omega^2 m_{Cu} - 2k\omega^2 m_O + \omega^4 m_O m_{Cu} - 2k^2 \\ &= \omega^2 [\omega^2 m_O m_{Cu} - k(m_{Cu} + 2m_O)] \end{aligned} \quad (2.37)$$

from here we obtain the uninteresting  $\omega^2 = 0$  and

$$\omega^2 = \frac{k(m_{Cu} + 2m_O)}{m_O m_{Cu}} \quad (2.38)$$

This is the frequency of the asymmetric (infrared) vibrational mode, denoted by  $\omega_{ir}$  in (2.3). Summarizing this part, we have found the dependence of the phonon frequencies  $\omega_{ir}$  and  $\omega_R$  with the atomic masses for the oxygen  $m_O$  and copper  $m_{Cu}$  atoms in the following way

$$\omega_R = \sqrt{\frac{k}{m_O}} \quad (2.39)$$

$$\omega_{ir} = \sqrt{\frac{k(m_{Cu} + 2m_O)}{m_O m_{Cu}}} \quad (2.40)$$

for some constant  $k$ . From here we identify the reduced masses for each vibrational mode<sup>4</sup>

$$m_R \equiv m_O \simeq 16.0 \text{ u} \simeq 2.6568 \times 10^{-26} \text{ kg} \quad (2.41)$$

$$m_{ir} \equiv \frac{m_O m_{Cu}}{m_{Cu} + 2m_O} \simeq 10.64 \text{ u} \simeq 1.7668 \times 10^{-26} \text{ kg} \quad (2.42)$$

From equations (2.8, 2.39, 2.40) it can be seen that an oxygen isotope substitution  $^{16}\text{O} \rightarrow ^{18}\text{O}$  amounts to a change in the frequencies ( $\omega_{ir}$ ,  $\omega_R$ ) and the coupling constants ( $\lambda_{ir}$ ,  $\lambda_R$ ). Denoting as  $\omega^{(16)}$  and  $\omega^{(18)}$  the phonon frequencies for a cluster

---

<sup>4</sup>We use  $m_{Cu} = 63.546 \text{ u}$ ,  $m_{^{16}\text{O}} = 15.995 \text{ u}$  and  $m_{^{18}\text{O}} = 17.999 \text{ u}$ .

with  $^{16}\text{O}$  and  $^{18}\text{O}$  respectively, we can find the ratios

$$\omega_{ir}^{(16)}/\omega_{ir}^{(18)} = \sqrt{\left(\frac{m_{18O}}{m_{16O}}\right) \left(\frac{m_{Cu} + 2m_{16O}}{m_{Cu} + 2m_{18O}}\right)} \quad (2.43)$$

$$\simeq 1.039 \quad (2.44)$$

$$\omega_R^{(16)}/\omega_R^{(18)} = \sqrt{\frac{m_{18O}}{m_{16O}}} \quad (2.45)$$

$$\simeq 1.061 \quad (2.46)$$

Similarly, for the coupling constants  $\lambda_{ir}$  and  $\lambda_R$ , from (2.8), we can observe that

$$\lambda_{ir}^{(16)}/\lambda_{ir}^{(18)} = \sqrt{\frac{m_{18O}\omega_{ir}^{(18)}}{m_{16O}\omega_{ir}^{(16)}}} \simeq 1.0407 \quad (2.47)$$

and equivalently for the Raman coupling constant

$$\lambda_R^{(16)}/\lambda_R^{(18)} = \sqrt{\frac{m_{18O}\omega_R^{(18)}}{m_{16O}\omega_R^{(16)}}} \simeq 1.0299 \quad (2.48)$$

Summarizing, to model an isotopic substitution  $^{16}\text{O} \rightarrow ^{18}\text{O}$  we need to adjust the vibrational frequencies and coupling constants according to equations (2.43-2.48)

## 2.5 Isotopic shifts

As is customary in optical spectroscopies we will consider the relative isotopic shift  $\Delta_i$  for an excited state  $i$  as

$$\Delta_i = \frac{\omega_i(^{16}\text{O}) - \omega_i(^{18}\text{O})}{\omega_i(^{16}\text{O})} \times 100 \quad (2.49)$$

where the energies  $\omega_i$  are calculated relative to the corresponding ground state. From this definition, using (2.39, 2.40), we can calculate the isotopic shift predicted by harmonic potentials for the Raman and infrared modes:

$$\Delta_R = 1 - \frac{\omega_R(^{18}\text{O})}{\omega_R(^{16}\text{O})} \times 100 = 5.75\% \quad (2.50)$$

$$\Delta_{ir} = 1 - \frac{\omega_{ir}({}^{18}\text{O})}{\omega_{ir}({}^{16}\text{O})} \times 100 = 3.75\% \quad (2.51)$$

Strong deviations from these values are indicative of a more complex behaviour.

For the ground state we define the energy isotopic shift  $\Delta_g$  in a similar way but with the energies measured relative to the uncoupled system, that is, the system with  $\lambda_{ir} = \lambda_R = 0$ ,

$$\Delta_g = \frac{\Delta\omega_g({}^{16}\text{O}) - \Delta\omega_g({}^{18}\text{O})}{\Delta\omega_g({}^{16}\text{O})} \times 100 \quad (2.52)$$

where  $\Delta\omega_g \equiv \omega_g - \omega_g(\lambda_{ir} = 0, \lambda_R = 0)$ . For the calculation of  $\Delta_g$  it is essential to include the *zero point energy* in the phononic part (2.3) which is usually not taken into account.

## 2.6 Choice of parameters

To choose values for this model we take representative values guided from local-density approximations [34]. In particular Ref. [93], using a tight-binding model, reports a band energy of  $E_0 = 0.35$  eV and a hopping parameter of  $t = 0.43 - 0.74$  eV, for Cu(1)-O(4) sites. The on-site Coulomb repulsion in  $\text{La}_2\text{CuO}_4$ ,  $U$  is estimated to be in the range 4.0 – 10.5 eV, [94].

The bare phonon frequency for the Raman vibrational mode is fixed to the value found experimentally in optical and inelastic neutron scattering experiments for  $\text{YBa}_2\text{Cu}_3\text{O}_7$ , namely  $\omega_R = 500 \text{ cm}^{-1}$  [80, 79] and  $\omega_{ir}$  is chosen such that the ratio  $\omega_{ir}/\omega_R$  given by (2.39-2.40) hold, which in this case gives  $\omega_{ir} = 612.4 \text{ cm}^{-1}$ .

In order to consider the simplest possible model we make the further assumption of taking the on-site Coulomb repulsion in the copper and oxygen sites to be equal with no nearest neighbor Coulomb repulsion. We also use a single hopping parameter  $t$  and ignore hopping between the two oxygen sites. Since only the coupling between the asymmetric mode and the charge motion leads to a measurable lattice distortion, with two Cu–O bond lengths, we only consider the effect of the variation in the electron–lattice coupling constant with the antisymmetric mode,  $\lambda_{ir}$ , and we set the electron-lattice coupling with the symmetric mode,  $\lambda_R$ , as zero [27]. The inclusion of those considerations in the model, or other choices of parameters produce very similar results (e.g. [22, 27]). The relevant value for the coupling  $\lambda_{ir}$  is determined using equation 2.12; it is chosen such that the ground state has a maximum probability density at a  $u_{ir}$  that reproduces the observed lattice distortion of  $0.13 \text{ \AA}$  [50]. In this work we use the same parameters as in Refs. [28, 29, 30, 31], namely:



- On-site Coulomb repulsion for O(4) and Cu(1) sites:  $U = 7$  eV
- Nearest-neighbor hopping:  $t = 0.5$  eV
- Band energy for O(4) and Cu(1) sites:  $E_0 = 0.5$  eV
- Bare phonon frequency for the Raman mode:  $\omega_R = 500$  cm<sup>-1</sup>
- Bare phonon frequency for the infrared mode:  $\omega_{ir} = 612.4$  cm<sup>-1</sup>

As previously stated, some variation in the parameter space has been explored without changes in the basic phenomenology. Table 2.1 shows the parameters for this model used in other publications<sup>5</sup>.

Reference	$U$ (eV)	$\epsilon$ (eV)	$t$ (eV)	$\omega_{ir}$ (cm <sup>-1</sup> )	$\omega_R$ (cm <sup>-1</sup> )
[18]	7.0	0.5	0.5	600	500
[22, 27]	4.44	0.307	0.634	477.7	576
[28, 29, 30, 31]	7.0	0.5	0.5	612.4	500
[32]	4.44	0.307	0.634	600	500

Table 2.1: Parameters for the model hamiltonian (2.1) used in other publications.

---

<sup>5</sup>It seems that the reported values for the phonon frequencies in Refs. [22, 27] are erroneous since they show  $\omega_R > \omega_{ir}$  and they are inconsistent from what can be observed, for example, in Fig. 1 of Ref. [22] at  $\lambda_{ir} = 0$ .



## Chapter 3

# Cluster distortion and bipolaron formation

We performed a series of diagonalizations of the hamiltonian matrix (2.1) using the parameters described in section 2.6 with a variable infrared charge-lattice coupling,  $\lambda_{ir}$ . We took  $\lambda_{ir}$  values in the representative range from 0 eV to 0.25 eV. This range allowed us to explore the behaviour of the system in the small, middle and strong coupling regimes. Besides the eigenvalues and eigenvectors of the hamiltonian we also calculated the mean phonon number with their dispersions and the projections into phonon coordinates ( $u_{ir}, u_R$ ) (see section 2.2).

In this chapter we turn our attention to the ground and first excited states of the system since only the first excitation in the (2.1) hamiltonian has a sufficiently low energy to be significantly occupied in the temperature range where the pseudogap phase is present. All other excitations have an energy above  $T = \omega_i/k_B \sim 550$  K (see Figure 4.2). First we calculate the difference in Cu-O bond lengths (if any) as a function of the  $\lambda_{ir}$  coupling parameter. With this we can find the  $\lambda_{ir}$  value that reproduces the 0.13 Å observed cluster distortion [38]. From the projection into phonon coordinates we can observe whether this distortion is static or dynamic for different  $\lambda_{ir}$  values [18]. The presence of a dynamic cluster distortion signals a correlated movement between atomic centers and charged particles, that is, it signals polaronic behaviour. The difference between the ground state energy in the absence of charge-lattice interaction ( $\lambda_{ir} = 0$ ) and its value for the coupling value where this polaronic behaviour sets can be identified as the *bipolaron binding energy*. We estimate this binding energy for the experimentally relevant  $\lambda_{ir}$  value and compare it to other calculations. Finally we model an isotopic oxygen substitution  $^{16}\text{O} \rightarrow ^{18}\text{O}$  and calculate its effects in the bipolaron binding energy.

### 3.1 Cu(1)-O(4) local distortion

The wavefunction projection into phonon coordinates (2.21) gives information about the coordinates of the three atoms in the  $\text{CuO}_2$  cluster. In particular, the infrared phonon coordinate  $u_{ir}$  is directly proportional to the bond distortion in the  $\text{CuO}_2$  cluster,  $d$ , as shown in (2.12). Since the ground state has zero Raman phonons and we have set  $\lambda_R = 0$ , its projection into  $u_R$  will remain unchanged and given by a simple gaussian distribution. Thus, setting  $u_R = 0$ , we projected the ground state into  $u_{ir}$  for different  $\lambda_{ir}$  values. In the left panel of Figure 3.1 we show a plot of these projections. The projection has a gaussian shape for  $\lambda_{ir} = 0$  however, as  $\lambda_{ir}$  increases it smoothly develops into two separated peaks. For a small range in the middle coupling values there are clearly two peaks but they are not separated. Since the system will tend to be near the maximum values of this projections this results can be interpreted as follows: in the small coupling range the bond distances remain equal albeit with an increased uncertainty; in the middle coupling range two Cu-O distances develop but the system can *tunnel* between them, that is, the distortion is *dynamic*; finally in the strong coupling range the two peaks are fully separated and the distortion becomes *static*. Only in the small range  $\sim 0.12 - 0.16$  eV the bond distortion has set in and it is dynamical in nature.

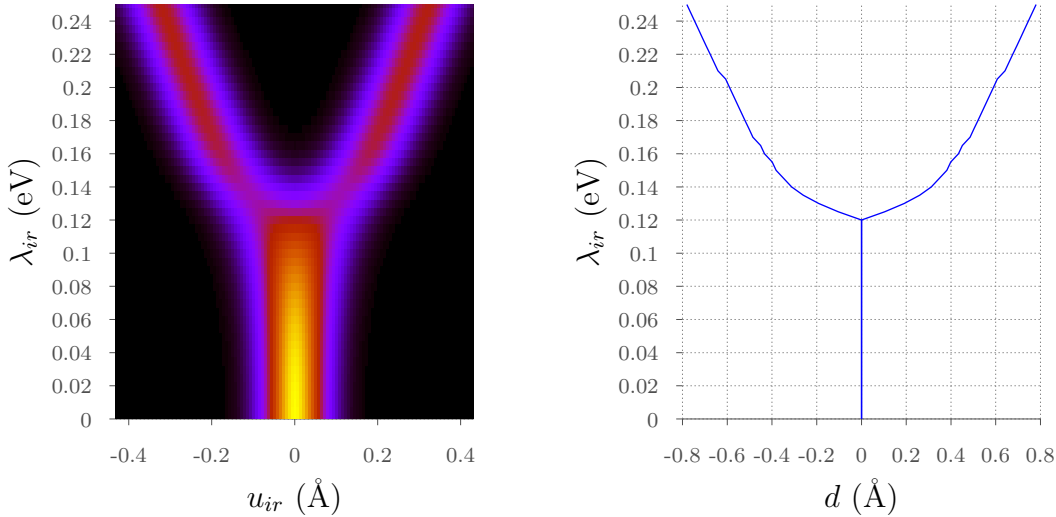


Figure 3.1: Projection into phonon coordinates (left panel) and calculated cluster distortion  $d$  (right panel) for different  $\lambda_{ir}$  coupling values with  $u_R = 0$ .

In the right panel of figure 3.1 we show the cluster distortion  $d$  assuming the

system is found in a maximum value of the projection into phonon coordinates. We observe that the distortion only sets in for  $\lambda_{ir} > \sim 0.12$  eV and monotonically increases with  $\lambda_{ir}$ . The two branches in this plot represent the two possible cluster distortions with the longer distance being in either of the CuO bonds. The measured cluster distortion of  $\sim 0.13$  Å [38] is reproduced in the intermediate coupling values. In particular,  $\lambda_{ir} = 0.1263$  eV reproduces that distortion.

The first excitation is an (antisymmetric) infrared-active state with one infrared phonon. Contrary to the ground state, the antisymmetry of this excitation implies that it is zero at  $u_{ir} = 0$  for all  $\lambda_{ir}$ . Also, the calculations show that increasing  $\lambda_{ir}$  reduces the energy of this excitation asymptotically to zero (see Figure 4.2) increasing its natural length scale. In Figure 3.2 we show the ground and first excited states projected into phonon coordinates ( $u_R, u_{ir}$ ) for  $\lambda_{ir}$  values in the weak, middle and strong coupling regimes. The projection along  $u_R$ , as previously stated, is a simple gaussian in all cases. In the middle coupling regime, with  $\lambda_{ir} = 0.1263$  eV, there are clearly two peaks present although, for the ground state, they are not fully separated. For large coupling values the two peaks are fully separated in both states (static distortion) and the projections become very similar.

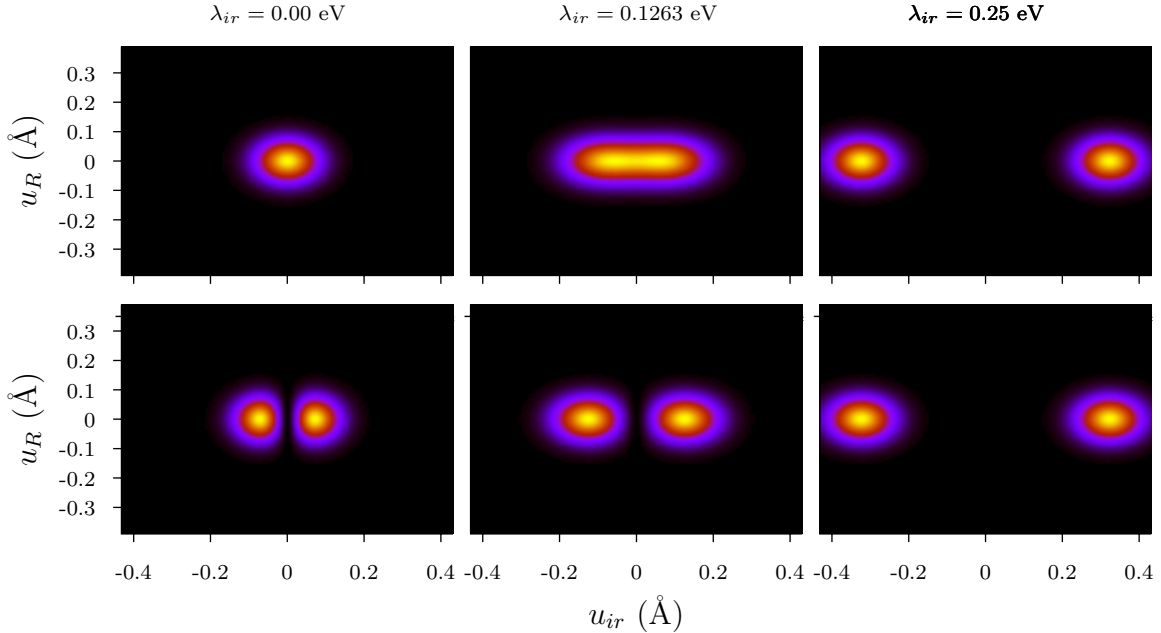


Figure 3.2: Projection into phonon coordinates for the ground (top) and first excited (bottom) states for three different values of the coupling parameter  $\lambda_{ir}$ .

The polaron-tunneling energy  $\omega_1$ , at the relevant  $\lambda_{ir} = 0.1263$  eV is  $141.39 \text{ cm}^{-1}$ ,

corresponding to a characteristic temperature  $T = \hbar\omega_1/k_B \sim 204$  K. Thus the atomic motion in the cluster, in the temperature range where the pseudogap is present, can be described by a two-level Hamiltonian  $\tilde{H} = (\omega_1/2)\sigma_z$ , such that  $\tilde{H}|\psi_1\rangle = +(\omega_1/2)|\psi_1\rangle$  and  $\tilde{H}|\psi_0\rangle = -(\omega_1/2)|\psi_0\rangle$ , where  $\sigma_z$  is a Pauli spin matrix and  $|\psi_0\rangle, |\psi_1\rangle$  denote the (symmetric) ground state and (antisymmetric) first excited state, respectively, separated by a *polaron tunneling* energy  $\hbar\omega_1$  [38].

## 3.2 Bipolaron binding energy

The energy of the ground state also changes with the coupling parameter  $\lambda_{ir}$ . The change in energy between the coupled and uncoupled systems,  $\Delta\omega_g$ , can be identified, in the region where there are bipolaronic objects present, as the *bipolaron binding energy*. In figure 3.3 we show the dependence of  $\Delta\omega_g$  with  $\lambda_{ir}$ .

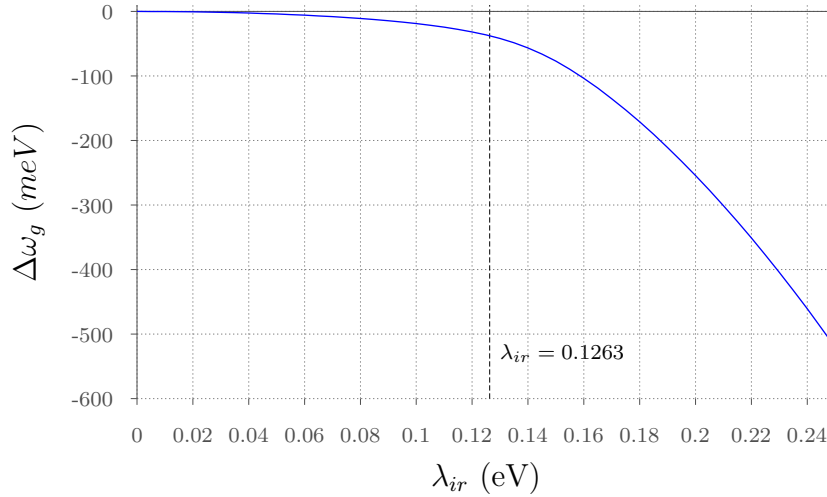


Figure 3.3: Bipolaron formation energy as a function of the  $\lambda_{ir}$  coupling. The vertical line is drawn at the relevant value  $\lambda_{ir} = 0.1263$  eV.

We observe a monotonical behaviour with a small change in the weak coupling regime becoming stronger with greater coupling values. In particular, for the  $\lambda_{ir} = 0.1263$  eV value, which reproduces the observed distortion, we find  $\Delta\omega_g \sim 38$  meV. This value compares favorably with the value obtained from femtosecond time-domain spectroscopy ( $\sim 45$  meV) for  $\text{YBa}_2\text{Cu}_3\text{O}_7$  [95]. We also find that if we consider a smaller electron-lattice coupling such that the distortion is  $0.08$  Å ( $\lambda_{ir} = 0.124$  eV),

as that observed for in plane Cu(2)-O in  $\text{La}_{1.85}\text{Sr}_{0.15}\text{CuO}_4$  [15], we obtain  $\Delta\omega_g \sim 35$  meV, which is also comparable to estimates for the pseudogap formation energy in this system (see Fig. 4b in [96]).

Furthermore, we calculated the isotopic shift,  $\Delta_g$ , of  $\omega_g$  under the  $^{16}\text{O} \rightarrow ^{18}\text{O}$  substitution as defined in (2.52). Figure 3.4 shows  $\Delta_g$  as a function of  $\lambda_{ir}$ . Contrary to other isotopic shifts, it does not change sign, however it shows a maximum in the middle coupling regime, reminiscent of the maxima, minima and inflection points in the isotopic shifts of all other excitations and falls below its starting point for large  $\lambda_{ir}$  values. For  $\lambda_{ir} = 0.1263$  eV we predict an isotopic shift of  $\sim 9.2$  % which is slightly larger than the uncoupled value of  $\sim 7.2$  %.

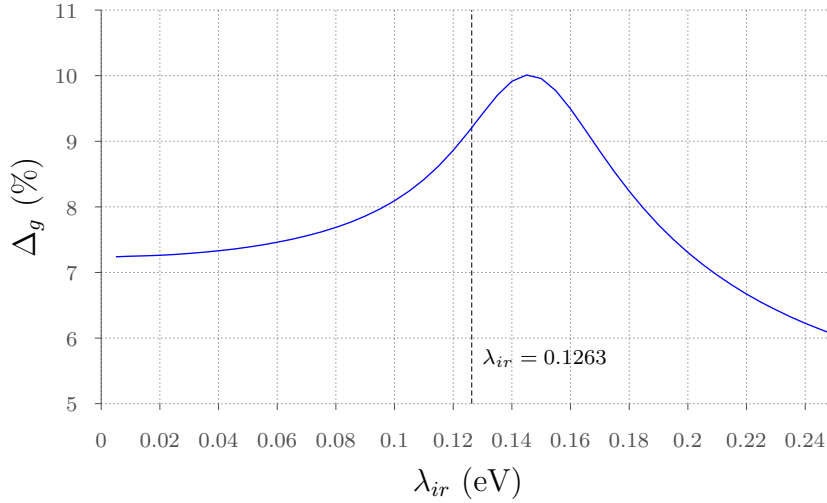


Figure 3.4: Isotopic shift of the bipolaron formation energy. The vertical line is placed at the relevant value  $\lambda_{ir} = 0.1263$ .





# Chapter 4

## Infrared spectra

In this chapter we present some general observations and discuss with more detail the infrared-active excitations. We start with section 4.1 describing the general nature of the different excitations. In section 4.2 we analyze some features that should be present in the infrared spectra followed, in section 4.3, by a description of the effects that the isotopic  $^{16}\text{O} \rightarrow ^{18}\text{O}$  substitution has in the spectra. Finally we conclude in section 4.4 with some observations about the projections into the phonon coordinates of these infrared-active states. We defer to appendix A some specific details about the calculations, such as the algorithm used and the numerical errors introduced by the truncation in the basis.

### 4.1 Classification of the excitations

As previously noted in section 2.1, only for zero charge-lattice couplings the eigenstates of the many-body Hamiltonian (2.1) can be described as a direct product of an electronic and a phononic state, that is, eigenstates of the full hamiltonian  $H$  are products of eigenstates of  $H_{el}$  and  $H_{ph}$  respectively. In this uncoupled scenario the phonon number operators  $b_R b_R^\dagger$  and  $b_{ir} b_{ir}^\dagger$  have integer values with zero dispersion. Increasing the value of the coupling parameters produces eigenstates with different mean phonon values and some finite dispersion producing eigenstates that can not be separated as a product of phononic and electronic states. However, the deviation from this behaviour is smooth in the coupling parameter  $\lambda_{ir}$ . That is, a hamiltonian with a small  $\lambda_{ir}$  value will have only slightly different eigenstates from the uncoupled hamiltonian. These slightly mixed eigenstates in the small coupling regime can be thought of as largely *phononic* or *electronic* in nature. For larger coupling values the eigenstates are very different from their uncoupled counterparts. As an illustration

of this we show, in figure 4.1, the first electronic excitation for different  $\lambda_{ir}$  values,  $\psi_{el}(\lambda_{ir})$  projected unto itself for the uncoupled system,  $\psi_{el}(\lambda_{ir} = 0)$ . From this projection we can see that for small coupling values  $\psi_{el}$  remains largely unchanged, that is, it remains *electronic* in nature. In the middle coupling regime the change is the strongest with the projection approaching asymptotically to zero at large couplings. The vertical line in 4.1 at  $\lambda_{ir} = 0.1263$  eV, as discussed in section 3.1, represents the  $\lambda_{ir}$  value that reproduces the experimentally observed cluster distortion of  $0.13$  Å. At this coupling value the electronic eigenstate has a projection unto its uncoupled counterpart near  $0.75$  which indicates that, although it has been somewhat changed, it remains mostly *electronic* in nature. Similar observations can be made for the rest of the excitations in this model. For this reason even though the eigenstates, for finite charge-lattice couplings, are not strictly electronic or phononic we will continue to refer to them as such since that interpretation remains useful in the regime of interest to us. Given the possibility of making such a distinction for the different excitations we will discuss *phononic* and *electronic* excitations separately in this and the next chapters respectively.

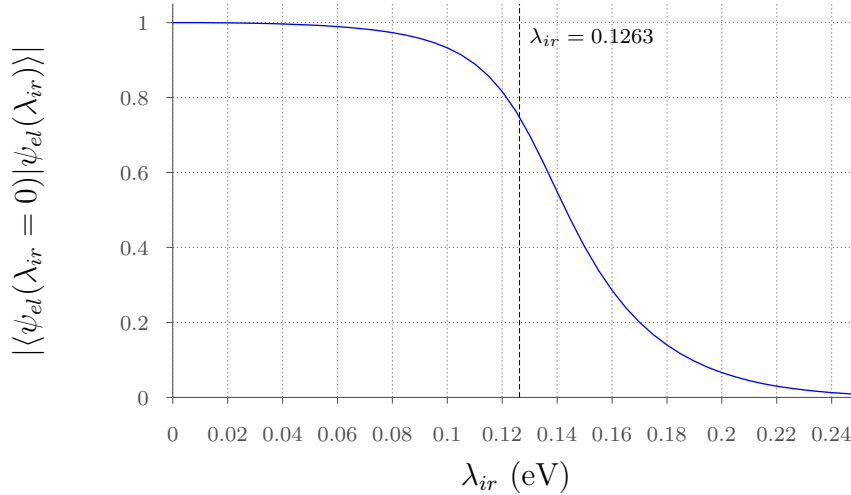


Figure 4.1: Projection of the first *electronic* state with itself at  $\lambda_{ir} = 0$ . The vertical line denotes the experimentally relevant value  $\lambda_{ir} = 0.1263$  eV.

Since we are setting the charge-lattice coupling parameter to the symmetrical (Raman) vibrational mode ( $\lambda_R$ ) as zero and these excitations are unchanged by an increase in  $\lambda_{ir}$ , all eigenstates will have a definite eigenvalue for the Raman number operator  $b_R^\dagger b_R$ . An excitation which, at  $\lambda_{ir} = 0$ , has an eigenvalue of zero for the

infrared number operator  $b_{ir}^\dagger b_{ir}$  and for the electronic part of the hamiltonian  $H_{el}$  (i.e. it is a pure *Raman* excitation with no other components) will remain completely unchanged with a variation in  $\lambda_{ir}$ . We will omit any further discussion about these excitations and ignore them for the rest of this thesis.

## 4.2 Infrared spectra

The Peierls-Hubbard model (2.1) applied to the O(4)-Cu(1)-O(4) cluster in  $\text{YBa}_2\text{Cu}_3\text{O}_7$  should be able to predict some features of the c-axis infrared spectra by looking at its infrared-active excitations. An excitation is infrared-active only when it has a opposite parity to the ground state. At  $\lambda_{ir} = 0$  the excitations are harmonic and have a opposite parity if the number of infrared phonons is even or odd, this means that only the excitations with an odd number of infrared phonons are infrared-active. Furthermore, since the coupling  $\lambda_{ir}$  can be varied smoothly, the hamiltonian eigenstates will not change parity as a function of  $\lambda_{ir}$  so it can be concluded that the infrared-active excitations, for any  $\lambda_{ir}$ , will be those that, at  $\lambda_{ir} = 0$ , have an *odd* number of phonons.

Figure 4.2 shows the infrared excitations for a representative range of  $\lambda_{ir}$  values. For  $\lambda_{ir} = 0$  we have excitations corresponding to the phononic part of the hamiltonian alone. As can be observed, the behaviour of each excitation depends on the number of infrared phonons at zero coupling. The number of Raman phonons only displaces the excitation in multiples of  $\omega_R = 500 \text{ cm}^{-1}$ . That is, all the red lines in Fig. 4.2 correspond to one infrared phonon and, in ascending order, have zero, one and two Raman phonons. This is similarly true for the excitations with two (green lines) and three (blue lines) infrared phonons. Notice that the excitations with two infrared phonons are not infrared-active since they have the same symmetry as the ground state.

All the infrared excitations reach a lower energy asymptotically at large  $\lambda_{ir}$  but only the state excitations with two infrared phonons have a minimum. The excitations with one infrared phonon decrease in energy converging to the Raman energies  $(0, \omega_R, 2\omega_R \dots)$ . However the excitations with two and three infrared phonons converge to the infrared energies  $(\omega_{ir}, 2\omega_{ir}, 3\omega_{ir} \dots)$ . This recovery of an harmonic behaviour at large  $\lambda_{ir}$  is similar to what was discussed in section 3.1 for the ground and first excited states which can be interpreted as a recovery of the harmonic behaviour but with a displaced equilibrium position.

It is interesting to notice that the infrared spectra at  $\lambda_{ir} = 0 \text{ eV}$  and at the relevant coupling,  $\lambda_{ir} = 0.1263 \text{ eV}$ , are very similar albeit with some noticeable differences. The peak centered at  $612.4 \text{ cm}^{-1}$  seems to be slightly shifted to  $641.4 \text{ cm}^{-1}$  with an

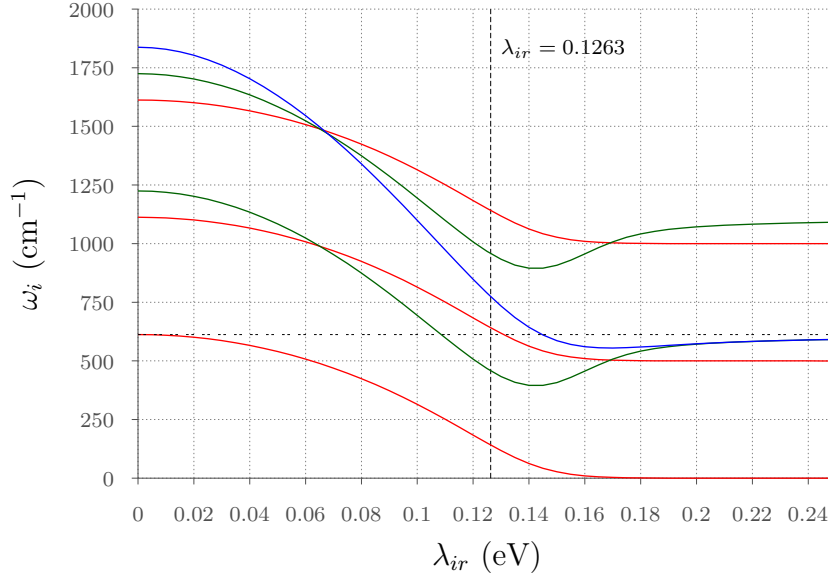


Figure 4.2: Infrared-active excitations as a function of electron-lattice coupling. The red, green and blue lines denote excitations which, initially, have one, two and three infrared phonons respectively. The horizontal dashed line is placed at the first infrared-active excitation  $\omega_i = 612.4 \text{ cm}^{-1}$  as a guide to the eye.

asymmetry produced by the excitation with three infrared phonons at  $774.2 \text{ cm}^{-1}$  (see inset of Fig. 2 in [18] and Fig. 2 in [22]). It should be noted that calculations using a rigid double-well potential for the O(4)-Cu(1)-O(4) cluster are unable to produce this asymmetry. Also in the  $\lambda_{ir} = 0.1263 \text{ eV}$  case there is an additional excitation at  $142.4 \text{ cm}^{-1}$  which has not yet been observed since other absorption processes in this range, e. g. a large Drude contribution in the D. C. conductivity, difficult its detection.

### 4.3 Isotopic shifts

We also calculated the infrared spectra change under the  $\text{O}^{16} \rightarrow \text{O}^{18}$  isotopic substitution and computed the corresponding isotopic shift, as defined by (2.49), for each excitation. In the top panel of Figure 4.3 we show the isotopic shift for the first infrare-active excitation and in the bottom panel the isotopic shifts for the excitations with two (red line) and three (blue line) infrared phonons as well as the state with one infrared plus one Raman phonon (red line).

As expected, all isotopic shifts start at the harmonic value which is 3.75% for

the pure infrared excitations and 4.65% for the excitation with one infrared plus one Raman phonons. For large  $\lambda_{ir}$  values the isotopic shifts of the infrared excitations with two and three phonons return asymptotically to the infrared harmonic value of 3.75% but the isotopic shift of the excitation with one infrared plus one Raman phonons converges to the Raman value of 5.75%. This behaviour for large  $\lambda_{ir}$  is a consequence of these excitations converging to either  $\omega_{ir}$  or  $\omega_R$ , as pointed out earlier. There is some variation of the isotopic shifts in the intermediate coupling regime but they always remain positive. It is interesting to notice that isotopic shift of the excitations with 3 infrared phonons and 1 infrared plus 1 Raman phonon have a minimum very close to the relevant coupling  $\lambda_{ir} = 0.1263$  eV.

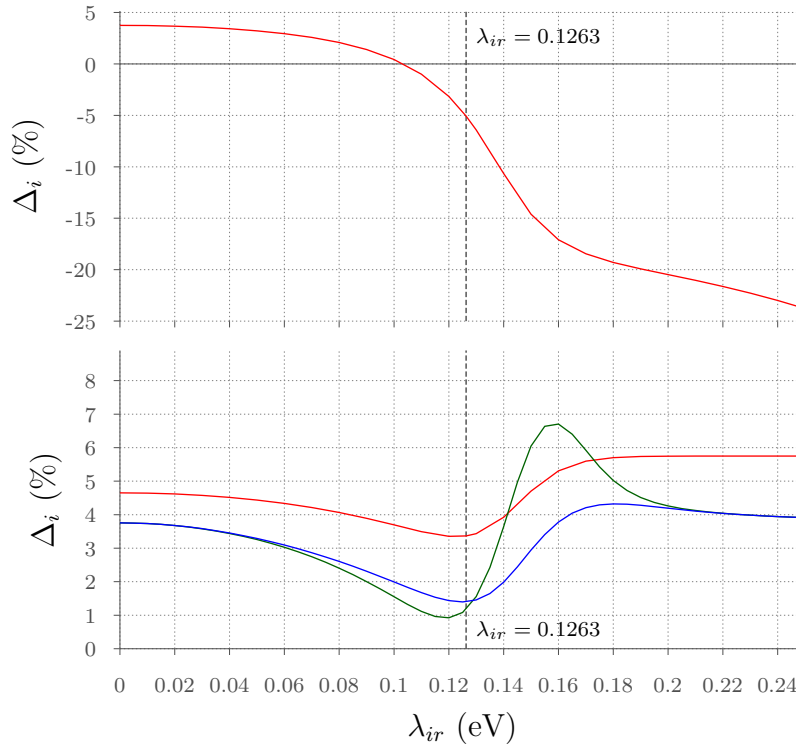


Figure 4.3: Isotopic shifts for the three main different infrared excitations. The top panel corresponds to the first infrared-active excitations. In the bottom panel the red line corresponds to the excitation with one infrared and one Raman phonon; the green and blue lines to the excitations with two and three infrared phonons respectively.

The first infrared excitation is peculiar since it has a negative isotopic shift for  $\lambda > \sim 0.1$  eV with a value of  $\sim -5.2\%$  for  $\lambda_{ir} = 0.1263$  eV. This negative isotopic

shift is a signal of polaronic behaviour in the system since harmonic and anharmonic potentials all predict positive isotopic shifts [32, 97]. For large coupling values this isotopic shift remains negative but seems to stabilize near 25% however, there could be some numerical instabilities in this specific isotopic shift attributable to float-point arithmetic limitations in the calculations since we are dealing with numbers very close to zero<sup>1</sup>.

In Table 4.1 we show the calculated energies for these excitations in the  $^{16}\text{O}$  and  $^{18}\text{O}$  cases as well as the isotopic shift  $\Delta_i$  for the  $\lambda_{ir} = 0.1263$  eV case. It can be seen that all the shifts are smaller than the harmonic prediction. However the strongest deviation is in the eigenstate with one infrared phonon where  $\Delta_i$  is negative.

Excitation	$\omega_i^{(16)} \text{ (cm}^{-1}\text{)}$	$\omega_i^{(18)} \text{ (cm}^{-1}\text{)}$	$\Delta_i \text{ (\%)}$	Harmonic (%)
1 infrared	141.39	148.56	-5.07	3.75
1 infrared and 1 Raman	641.39	619.81	3.36	4.65
2 infrared	457.60	452.25	1.17	3.75
3 infrared	774.25	763.41	1.40	3.75

Table 4.1: Energies and isotopic shifts for the three main infrared excitations in the  $\lambda_{ir} = 0.1263$  eV case compared with the harmonic prediction.

## 4.4 Projection into phonon coordinates

As a further visualization of the deviation and recovery of harmonic behaviour with  $\lambda_{ir}$  we projected the eigenstates corresponding to two and three infrared phonons into  $(u_{ir}, u_R)$ . In Figure 4.4 we show a plot of this projection for the three representative coupling values  $\lambda_{ir} = 0, 0.1263$  and  $0.25$  eV.

It is illustrative to compare this plot with Figure 3.2 showing a similar comparison for the ground and first excited states. In all cases, at  $\lambda_{ir} = 0$  eV the projection is what can be expected for an harmonic oscillator; it is a simple gaussian when the number of phonons is zero and it has an increasing number of nodes corresponding to the number of phonons in the excitation. For large  $\lambda_{ir}$  the projection of the excitations with two and three infrared phonons become very similar, analogous to the similarity between the ground and first excited states. It was shown in Figure 4.2 that for large  $\lambda_{ir}$  the energy of the states with two and three infrared phonons converge to the energy of one infrared phonon,  $\omega_{ir}$ . In Figure 4.4 we can see that the projections of these states, for large  $\lambda_{ir}$ , is similar to two displaced harmonic states with just

<sup>1</sup>See section A.3 in the appendix

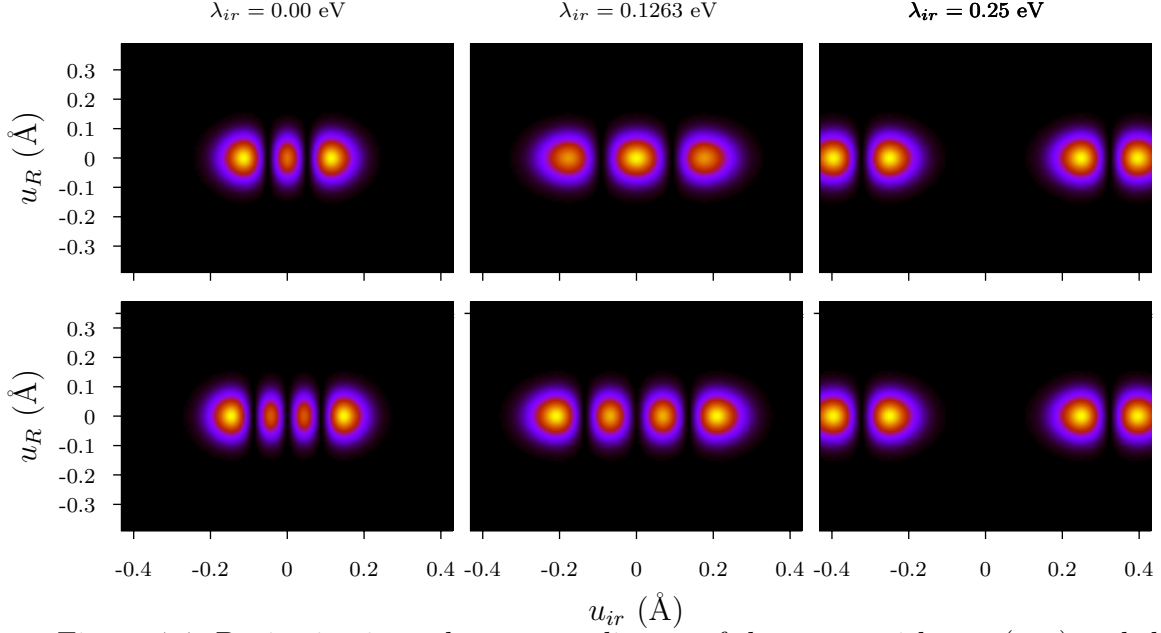


Figure 4.4: Projection into phonon coordinates of the states with two (top) and three (bottom) infrared phonons for three representative  $\lambda_{ir}$  values.

one infrared phonon. This is further evidence charge *freezing*, signaling an incipient ferromagnetism, and the distortions in the cluster becoming static.

Since the states with an *even* number of infrared phonons (and an even number of nodes in the  $u_{ir}$  projection) converge to states with an *odd* number of infrared phonons (with odd nodes), at some point in the  $\lambda_{ir}$  regime they must develop an additional node. It was shown in 3.1 that, for  $\lambda_{ir} = 0.1263$  eV, the ground state has already developed a partial peak separation that becomes complete only for  $\lambda_{ir} > 0.16$  eV. In contrast the excitation with two infrared phonons, at this same coupling, still has only one central peak that splits at larger coupling values.





# Chapter 5

## Electronic excitations

We now turn our attention to the other kind of excitations present in the model hamiltonian (2.1), namely, the *electronic* excitations. These excitations are those that, in the absence of charge-lattice coupling, arise from the  $H_{el}$  term (2.2). Since they do not have an opposing parity to the ground state, they are inactive in infrared and Raman spectroscopies but could be accessible by electronic probes such as ARPES<sup>1</sup>. It should be noted however that ARPES probes the *occupied* electronic states in a system and such an interpretation is difficult in our model.

Unlike  $H_{ph}$ , the electronic term  $H_{el}$  is not infinite dimensional since it depends only on the position of the charges in the atomic sites. Using the labelling convention stated in (2.23),  $H_{el}$  can be expressed as the following 9x9 matrix:

$$H_{el} \doteq \begin{pmatrix} U + 2E_0 & t & 0 & t & 0 & 0 & 0 & 0 & 0 \\ t & 0 & t & 0 & t & 0 & 0 & 0 & 0 \\ 0 & t & 2E_0 & 0 & 0 & t & 0 & 0 & 0 \\ t & 0 & 0 & 0 & t & 0 & t & 0 & 0 \\ 0 & t & 0 & t & U - 2E_0 & t & 0 & t & 0 \\ 0 & 0 & t & 0 & t & 0 & 0 & 0 & t \\ 0 & 0 & 0 & t & 0 & 0 & 2E_0 & t & 0 \\ 0 & 0 & 0 & 0 & t & 0 & t & 0 & t \\ 0 & 0 & 0 & 0 & 0 & t & 0 & t & U + 2E_0 \end{pmatrix} \quad (5.1)$$

This matrix is easily diagonalized to see that its first excited state has an energy of  $\sim 1376 \text{ cm}^{-1}$  above the ground state which is considerable higher than the phononic energies of 500 and  $612.4 \text{ cm}^{-1}$ .

---

<sup>1</sup>Angle Resolved Photo-Emission Spectroscopy

Since  $H_{el-ph}$  mixes electronic and phononic degrees of freedom, a change in the coupling parameter  $\lambda_{ir}$  also changes the properties of these excitations. Similar to the phononic excitations analyzed in the previous chapter these excitations do not remain eigenstates of  $H_{el}$  for  $\lambda_{ir} > 0$  however, as discussed in section 4.1, in the middle coupling regime they remain mainly electronic in nature so we continue to refer them as such.

In Figure 5.1 we show the energy of the three lowest electronic excitations as a function of  $\lambda_{ir}$ . All energies show a monotonically decreasing behaviour with  $\lambda_{ir}$ , reminiscent of the phononic excitations in Figure 4.2 with little change in the small and strong coupling regimes but considerable change is in the middle coupling regime. The first excitation starts at  $\sim 1376 \text{ cm}^{-1}$  for  $\lambda_{ir} = 0$  and converges to  $\sim 1122 \text{ cm}^{-1}$  for large  $\lambda_{ir}$ . The electronic excitation with one additional infrared phonon also converges to this energy. The presence of a Raman phonon rigidly increases the energies by  $\omega_R = 500 \text{ cm}^{-1}$  for every  $\lambda_{ir}$ .

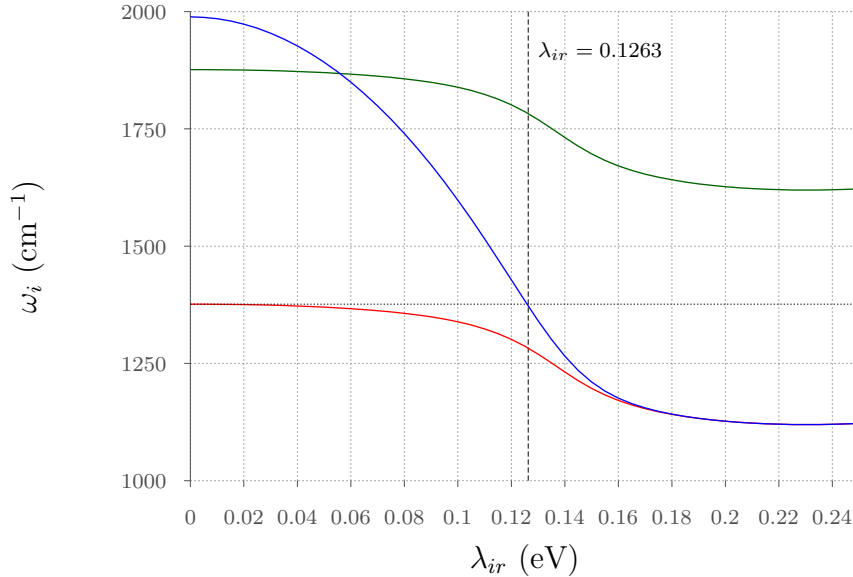


Figure 5.1: Energy of the electronic excitations as function of  $\lambda_{ir}$ . The red line corresponds to an electronic excitation with zero phonons, the blue line with one infrared phonon and the green line with one Raman phonon. The vertical line is placed at the relevant value  $\lambda_{ir} = 0.1263 \text{ eV}$ .

At  $\lambda_{ir} = 0.1263 \text{ eV}$  the first electronic excitation has the lower energy of  $\sim 1282 \text{ cm}^{-1}$  however the excitation with one additional infrared phonon has an energy of

$\sim 1373 \text{ cm}^{-1}$  which is very close to the  $\sim 1376 \text{ cm}^{-1}$  value for the first excitation at  $\lambda_{ir} = 0$ . Wa

## 5.1 Partial charge localization

We use (2.22) to find the probability  $P(e_1, e_2)$  of finding an excitation with the first and second charges at sites  $e_1$  and  $e_2$  respectively where  $e_i = 1, 3$  denotes a charge at the oxygen sites and  $e_i = 2$  at the copper site. In Figure 5.2 we show the probabilities for one charge in an oxygen and the other in the copper (top panel) as well as both charges in the opposite oxygen sites (bottom panel). The probabilities of finding both charges in the same site are very low, due to the large on-site Coulomb repulsion  $U = 7 \text{ eV}$ , so we omit a figure about them. It should be noted however that the double occupancy probabilities remain in the  $\sim 0.1\%$  range for the ground and first infrared excitations but are zero in the electronic excitation for all  $\lambda_{ir}$ . Since the cluster is symmetric some probabilities are equivalent:  $P(1, 2) = P(2, 1) = P(2, 3) = P(3, 2)$ ,  $P(1, 3) = P(3, 1)$  and  $P(1, 1) = P(3, 3)$ .

For all three eigenstates the general trend is similar; there is a monotonic increase in the probability of finding one charge in the oxygen and the other in the copper sites while the probability of both charges being in the opposite oxygen sites decreases. This can be interpreted as a partial charge localization in the cluster, although there is still some charge movement [98].

## 5.2 Projection into phonon coordinates

We also investigated the projection into phonon coordinates for the first electronic excitation in the model. In Figure 5.3 we show these projections for  $\lambda_{ir} = 0, 0.1263$  and  $0.25 \text{ eV}$  corresponding to values in the weak, middle and strong coupling regimes. Similar to the other excitations, the projection along  $u_R$  remains unchanged in the form of a gaussian function. At  $\lambda_{ir} = 0 \text{ eV}$  the projection along  $u_{ir}$  has also a gaussian shape however, for the coupling value that reproduces the cluster distortion ( $\lambda_{ir} = 0.1263 \text{ eV}$ ), it develops a double peak structure reminiscent of the ground state in Figure 3.2 although with more defined peaks. For large  $\lambda_{ir}$  the two peaks are completely separated each one similar to the  $\lambda_{ir} = 0 \text{ eV}$  case but displaced in origin. This behaviour at large coupling values is similar to what was observed for all the other excitations in which the uncoupled scenario is recovered with a displaced origin.

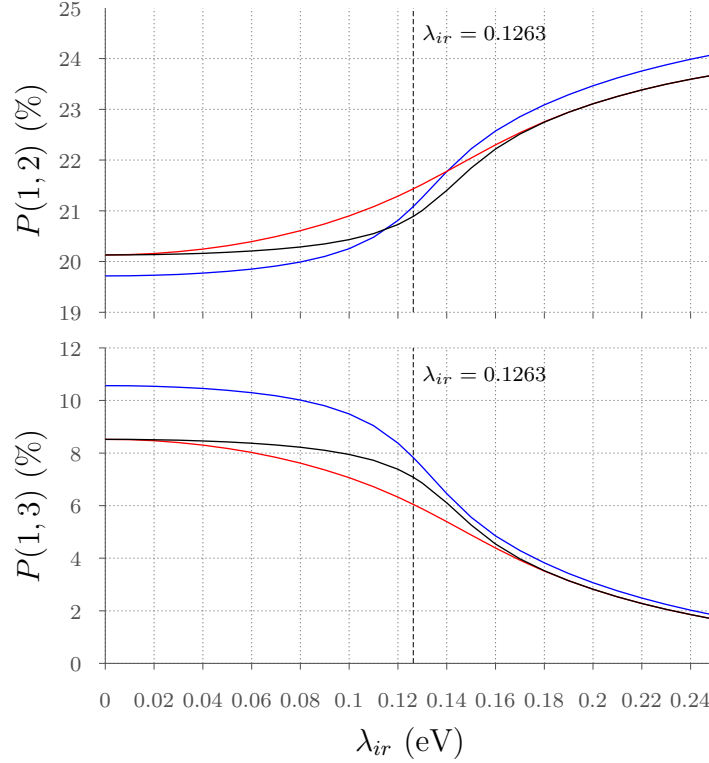


Figure 5.2: Probability of finding the system with one charge in an oxygen and the other at the copper (top panel) and both charges at opposing oxygen sites (bottom panel) as a function of  $\lambda_{ir}$ . The vertical line marks the relevant  $\lambda_{ir} = 0.1263$  eV value.

### 5.3 Isotopic shift

We also investigated the effect of an oxygen isotopic change  $^{16}\text{O} \rightarrow ^{18}\text{O}$  in the eigenvalues of the electronic excitations. In Figure 5.4 we show a plot of the isotopic shift  $\Delta_g$  as defined in (2.52) for the first electronic excitation as well as the excitation with an additional infrared phonon for a range of  $\lambda_{ir}$  values. Since the electronic excitations are unaffected by changes in the phonon energies when  $\lambda_{ir} = 0$  eV, the isotopic shift of the first electronic excitation is zero and the shift for the excitation with one additional infrared phonon is what could be expected from the harmonic behaviour of the system. Interestingly, the isotopic shift decreases to a minimum close to the relevant  $\lambda_{ir} = 0.1263$  eV value and then increases again becoming almost linear for  $\lambda_{ir} > 0.18$  eV.

For both excitations shown in Figure 5.4 the isotopic shift becomes negative in the

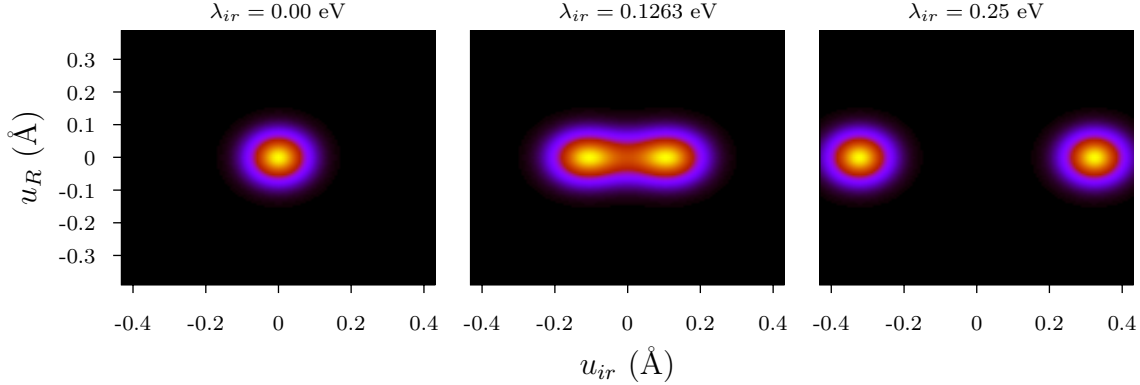


Figure 5.3: Projection into phonon coordinates of the electronic excitation for three representative  $\lambda_{ir}$  values.

middle coupling regime similarly to the first infrared excitation at these values (see top panel of Figure 4.3) although with a reduced magnitude. In contrast, for larger  $\lambda_{ir}$  these shifts seem to increase indefinitely not stabilizing to any value. Although the calculations seem to converge well in the  $\lambda_{ir}$  range we are considering, we should note that there could be some convergence issues at large  $\lambda_{ir}$  due to the truncation of the basis.

As mentioned section 1.5, the  $^{16}\text{O} \rightarrow ^{18}\text{O}$  isotopic effect on electronic excitations has been experimentally explored by ARPES. Gweon et al. [90] found a different isotope effect for nodal and antinodal excitations in optimally doped  $\text{Bi}_2\text{Sr}_2\text{CaCu}_2\text{O}_{8+\delta}$ . They found energy differences ranging approximately from -15 to 40 meV for nodal and antinodal excitations respectively. However, a later study by Douglas et al. [91] found a much smaller, and possibly negligible, isotope effect ranging from  $-0.9 \pm 0.4$  to  $2 \pm 3$  meV.

The interpretation of the electronic excitations observed by ARPES in terms of our simple model hamiltonian is not straightforward, however, we also find positive and negative isotopic effects that, in our case, corresponds to undistorted and distorted O(4)-Cu(1)-O(4) clusters respectively. In contrast with the work of Gweon et al. we predict a considerable smaller isotopic effect around  $\pm 1\%$ , which is in the 1-2 meV range. Although Douglas et al. claim to have observed a lack of isotopic effects on the electronic excitations, our prediction falls well into their experimental uncertainty prompting for more accurate ARPES studies in these samples.

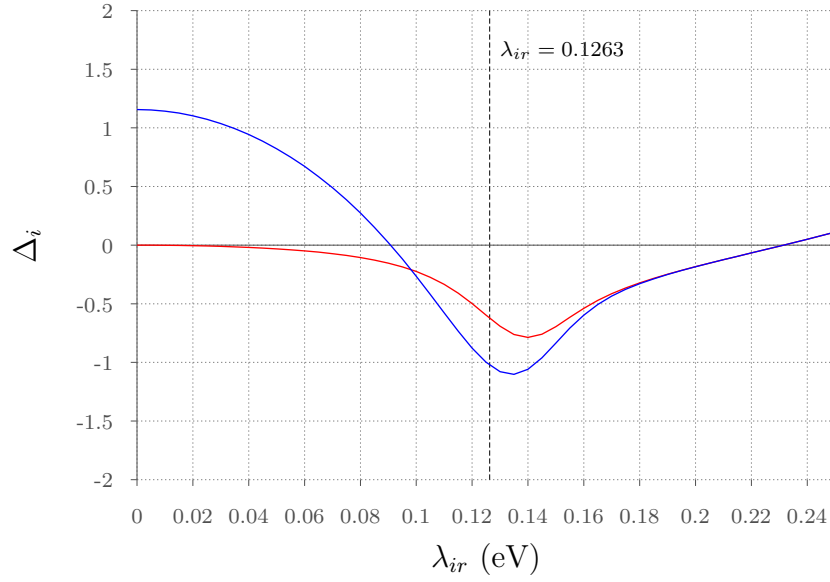


Figure 5.4: Isotopic shifts of the electronic excitations as a function of  $\lambda_{ir}$ . The red line corresponds to an electronic excitation with zero phonons, the blue line with one infrared phonon and the green line with one Raman phonon. The vertical line is placed at the relevant value  $\lambda_{ir} = 0.1263$  eV.

# Chapter 6

## Discussion and conclusions

In this thesis we have reviewed the evidence for the appearance of a dynamically inhomogeneous ground state in the pseudogap region in which the charge and lattice degrees of freedom are fundamentally coupled. In this state the charge-lattice coupling produce bipolaronic objects below the pseudogap onset temperature  $T^*$ . The manifestation of these objects in the lattice appears as dynamical local lattice distortions in regions in which the charge and lattice motion become correlated. The excitations of these bipolaronic objects exhibit different isotopic shifts depending on the nature of the excitation ranging from large negative to quasi-harmonic shifts. These peculiar shifts are consistent with experimental observations and might explain discrepancies in values determined by different techniques, as they probe different excitations depending on the time and spatial resolution of the specific technique. However, the role in the pairing of free fermions of these bipolaronic excitations, and enhancement of  $T_c$  is not yet known.

### 6.1 Validity of the Born-Oppenheimer approximation

It is interesting to note that, although the isotopic shifts of the ground state and lowest excitations can be either positive or negative, they all exhibit the strongest variations in the intermediate coupling regime where the eigenstates in the system are mixed and it is not possible to separate them into an *electronic* and a *lattice* part. It is in this intermediate regime, where the charge and lattice movements are intrinsically correlated, that the Born-Oppenheimer approximation ceases to be valid. An exact treatment, such as the one used in this work, is free from such an approximation,

however it is computationally expensive and only relatively small systems can feasibly be explored at the moment.

The importance of the intermediate coupling regime suggests a characteristic dynamical scale for the polaronic features in the cuprate superconductors. Other transition metals oxides as manganites and nickelates exhibit similar local lattice distortions however, the size of the distortion is larger in manganites ( $\sim 0.2 \text{ \AA}$ ) [99] and smaller in nickelates ( $\sim 0.05 \text{ \AA}$ ) [100] resulting also in different time scales. It is enticing to relate the particular dynamical time scale of the local lattice distortions with the presence of high-temperature superconductivity in cuprates but not in other transition metal oxides thus highlighting the relevance of model hamiltonians not relying on the adiabatic and anti-adiabatic approximations.

## 6.2 Multicomponent superconductivity

Finally, we would like to discuss the possible relevance of the bipolaronic behavior, derived from the simple Peierls-Hubbard Hamiltonian model (2.1) to high temperature superconductivity. The observation of a Fermi surface in photoemission experiments [101, 102] implies that, in addition to the bipolaronic objects (of bosonic character), there are also quasi-free fermions. As a function of doping the ratio of these two kinds of objects varies, yielding different characterizations of the ground state starting as an antiferromagnetic Mott insulator at zero doping, an inhomogeneous pseudogap phase where at least two different type of carriers coexist and ending in a Fermi-liquid metal in the overdoped region of the phase diagram. The fact that the highest  $T_c$  is realized in this pseudogap region suggests the importance of the bipolaron bosonic objects. However, their role in the pairing of free fermions and enhancement of  $T_c$  is not yet known. In order to understand this role, a natural extension of the model treated here is to couple the Hamiltonian (2.1) to an independent free fermion system  $H_A$  and find the corresponding excitations allowing exchange of the fermions involved in the bipolaronic objects with those in the free fermion part. In the spirit of the exact treatment of the bipolaronic subsystem, the simplest interaction between mobile fermions and charges forming part of a bipolaron is a linear hopping term. Such a term would allow the transfer of a single fermion from the mobile fermion to the bipolaron subsystems. In principle, in an exact treatment like this, the possibility of pair hopping would be implicitly included. That is not the case in a perturbative treatment, in which the single particle exchange (hopping) can be folded into the pair exchange (see [25]). If we consider the simplest free fermion system consisting only on two non interacting fermions in real space, with creation and annihilation operators



$a^\dagger$  and  $a$  respectively, the coupling of (2.1) to this system ( $H_A$ ) can be written as

$$H_A = E_A \sum_{\sigma,k=1,2} m_{\sigma,k} + t_A \sum_{\sigma} (a_{\sigma,1}^\dagger a_{\sigma,2} + a_{\sigma,2}^\dagger a_{\sigma,1}) + \lambda_A \sum_{i,k,\sigma} (c_{i,\sigma}^\dagger a_{k,\sigma} + a_{k,\sigma}^\dagger c_{i,\sigma}) \quad (6.1)$$

with  $i = 1, 2, 3$  labeling the sites in the  $\text{CuO}_2$  cluster and  $k = 1, 2$  the two sites for the free fermions. Here  $m_{\sigma,k} = a_{\sigma,k}^\dagger a_{\sigma,k}$  is the number operator in the free fermion subsystem,  $E_A$  its site energy and  $\lambda_A$  parametrizes its interaction with the  $\text{CuO}_2$  cluster. This approach still allows us to use an exact treatment, albeit missing the possible extended nature of the free fermion states. If a perturbative approach was used instead it could be possible to replace the free fermion subsystem by a full band in  $k$ -space. In addition, an onsite Coulomb repulsion term could be added to the free electron subsystem and still feasibly perform an exact diagonalization. In this case the basis set, considering the same number of phonons, is two orders of magnitude larger than the one used for the original Peirls-Hubbard Hamiltonian (2.1) but still within reach of modern computational resources.

In this model an increased projection of a given excitation on a double occupancy basis state of the free fermion part would be a signature of pairing mediated by the bipolaronic objects in the  $\text{CuO}_2$  cluster. Additionally, the role played by the antiferromagnetic background present at zero doping and its interaction with both the fermionic carriers and polaronic objects has to be addressed.



# Appendix A

## Computational details

In this appendix we give some details regarding the algorithms used for the calculations in this thesis as well as a couple of simple observations showing the adequacy of the size of the basis set used. The algorithm used is released under a GNU General Public License version 3 (GPLv3) and, at the time of this writing, it is freely accessible on the Internet [103].

### A.1 Algorithm

The first iterations of our calculations were made with a QR algorithm which is a full-matrix diagonalization procedure. The particular implementation was that provided by the *Eigen* C++ package [104]. The choice of this algorithm was mainly due to its accessibility and ease of use. However, the hamiltonian matrix is sparse, that is, most of its elements are zero. In fact, only about  $\sim 0.03\%$  of them are different from zero. Thus, it is more appropriate to use a diagonalization procedure optimized for sparse matrices.

Fortunately, there was sparse matrix support [105] in the popular Octave package [106] introduced during the timeframe of this project so we could switch to that implementation in the later stages. This implementation uses an interface to the ARPACK package [107] and is able to find the lowest eigenvalues and eigenvectors of a sparse matrix with drastically inferior computational resources compared to the QR algorithm.

The algorithm used for this thesis [103] is very simple. First it builds a hamiltonian matrix from (2.1) and afterwards it calls the sparse diagonalization routine implemented within Octave. The only non-trivial aspect is the mapping from the quantum number  $|e_1, e_2, ir, R\rangle$  (see section 2.1) to an integer  $l$  labelling the row/column in the

matrix. This mapping can be achieved as follows:

$$l = e_1 + 3(e_2 - 1) + 9 \text{ } ir + 9 \text{ } R(N_{ir} + 1) \quad (\text{A.1})$$

with  $N_{ir}$  being the total number of infrared phonons under consideration.

## A.2 Convergence

The basis includes up to 30 harmonic Raman and 30 harmonic infrared phonons. The truncation of the basis to a finite number of phonons could introduce inaccuracies, however we found this choice to be an adequate choice to ensure convergence in the few lowest energy states we are considering and electron-lattice couplings up to  $\sim 0.25$  eV<sup>1</sup>.

## A.3 Numerical instabilities

We performed an exact diagonalization of the Hamiltonian matrix with a basis of 8649 states using a QR algorithm [104]<sup>2</sup>.

---

<sup>1</sup>There is another numerical instability present in the calculation of the isotopic shift of the first excitation (see the top panel of figure 4.3) but this seems to be due to floating point errors in the calculations since all numbers are very close to zero.

<sup>2</sup>The hamiltonian (2.1) is a sparse matrix, so a more efficient approach is being taken in subsequent calculations, in extensions of this model, using Lanczos algorithm. In this work we used a QR algorithm because it was readily available and provided a large enough basis set to ensure convergence.

# Bibliography

- [1] J G Bednorz and K. A. Müller. Possible high  $T_c$  superconductivity in the Ba-La-Cu-O system. *Zeitschrift für Physik B Condensed Matter*, 64(2):189–193, June 1986.
- [2] R. Cava, R. van Dover, B. Batlogg, and E. Rietman. Bulk superconductivity at 36 K in  $\text{La}_{1.8}\text{Sr}_{0.2}\text{CuO}_4$ . *Physical Review Letters*, 58(4):408–410, January 1987.
- [3] M. Wu, J. Ashburn, C. Torng, P. Hor, R. Meng, L. Gao, Z. Huang, Y. Wang, and C. Chu. Superconductivity at 93 K in a new mixed-phase Y-Ba-Cu-O compound system at ambient pressure. *Physical Review Letters*, 58(9):908–910, March 1987.
- [4] Cuprate superconductors phase diagram. <https://en.wikipedia.org/wiki/File:Cuphasediag.png> 2009.
- [5] Tom Timusk and Bryan Statt. The pseudogap in high-temperature superconductors: an experimental survey. *Reports on Progress in Physics*, 62(1):61–122, January 1999.
- [6] N F Mott. The Basis of the Electron Theory of Metals, with Special Reference to the Transition Metals. *Proceedings of the Physical Society. Section A*, 62(7):416, 1949.
- [7] M. Gurvitch and A. Fiory. Resistivity of  $\text{La}_{1.825}\text{Sr}_{0.175}\text{CuO}_4$  and  $\text{YBa}_2\text{Cu}_3\text{O}_7$  to 1100 K: Absence of saturation and its implications. *Physical Review Letters*, 59(12):1337–1340, September 1987.
- [8] J Orenstein. Advances in the Physics of High-Temperature Superconductivity. *Science*, 288(5465):468–474, April 2000.
- [9] K a Müller. On the superconductivity in hole doped cuprates. *Journal of Physics: Condensed Matter*, 19(25):251002, June 2007.

- 
- [10] D N Basov. Electrodynamics of high- $T_c$  superconductors. *Reviews of Modern Physics*, 77(2):721–779, August 2005.
- [11] Nicola Poccia, Michela Fratini, Alessandro Ricci, Gaetano Campi, Luisa Barba, Alessandra Vittorini-Orgeas, Ginestra Bianconi, Gabriel Aeppli, and Antonio Bianconi. Evolution and control of oxygen order in a cuprate superconductor. *Nature materials*, 10(10):733–6, October 2011.
- [12] C. Chen, D. Werder, L. Schneemeyer, P. Gallagher, and J. Waszczak. Observation of oxygen-vacancy-ordered domains in oxygen-deficient single-crystal  $\text{YBa}_2\text{Cu}_3\text{O}_{6.7}$ . *Physical Review B*, 38(4):2888–2891, August 1988.
- [13] N.H. Andersen, B Lebech, and H.F. Poulsen. The structural phase diagram and oxygen equilibrium partial pressure of  $\text{YBa}_2\text{Cu}_3\text{O}_{6+x}$  studied by neutron powder diffraction and gas volumetry. *Physica C: Superconductivity*, 172(1-2):31–42, December 1990.
- [14] D. Mihailovic. Optical Experimental Evidence for a Universal Length Scale for the Dynamic Charge Inhomogeneity of Cuprate Superconductors. *Physical Review Letters*, 94(20):207001, May 2005.
- [15] A. Bianconi, N. Saini, A. Lanzara, M. Missori, T. Rossetti, H Oyanagi, H Yamaguchi, K Oka, and T Ito. Determination of the Local Lattice Distortions in the  $\text{CuO}_2$  Plane of  $\text{La}_{1.85}\text{Sr}_{0.15}\text{CuO}_4$ . *Physical Review Letters*, 76(18):3412–3415, April 1996.
- [16] D Rubio Temprano, J Mesot, S Janssen, K Conder, A Furrer, H Mutka, and K. Müller. Large Isotope Effect on the Pseudogap in the High-Temperature Superconductor  $\text{HoBa}_2\text{Cu}_4\text{O}_8$ . *Physical Review Letters*, 84(9):1990–1993, February 2000.
- [17] a Kaminski, S Rosenkranz, H M Fretwell, J C Campuzano, Z Li, H Raffy, W G Cullen, H You, C G Olson, C M Varma, and H Höchst. Spontaneous breaking of time-reversal symmetry in the pseudogap state of a high- $T_c$  superconductor. *Nature*, 416(6881):610–3, April 2002.
- [18] J. Mustre de Leon, I. Batistic, A.R. Bishop, SD Conradson, and S.A. Trugman. Polaron origin for anharmonicity of the axial oxygen in  $\text{YBa}_2\text{Cu}_3\text{O}_7$ . *Physical Review Letters*, 68:3236–3239, 1992.
- [19] M. Born and R. Oppenheimer. Zur Quantentheorie der Molekeln. *Annalen der Physik*, 389(20):457–484, 1927.

- [20] J. Bardeen, L. N. Cooper, and J. R. Schrieffer. Theory of Superconductivity. *Physical Review*, 108(5):1175–1204, December 1957.
- [21] Andrea Damascelli and Zhi-Xun Shen. Angle-resolved photoemission studies of the cuprate superconductors. *Reviews of Modern Physics*, 75(2):473–541, April 2003.
- [22] MI Salkola, AR Bishop, J. Mustre de Leon, and SA Trugman. Dynamic polaron tunneling in  $\text{YBa}_2\text{Cu}_3\text{O}_7$ : Optical response and inelastic neutron scattering. *Physical Review B*, 49:3671–3674, 1994.
- [23] a. Bussmann-Holder and H. Keller. Polaron formation as origin of unconventional isotope effects in cuprate superconductors. *The European Physical Journal B*, 44(4):487–490, May 2005.
- [24] D Mihailovic and V. Kabanov. Finite wave vector Jahn-Teller pairing and superconductivity in the cuprates. *Physical Review B*, 63(5):054505, January 2001.
- [25] Y. Bar-Yam. Two-component superconductivity. I. Introduction and phenomenology. *Physical Review B*, 43(1):359–377, January 1991.
- [26] A. Bianconi, N. L. Saini, S Agrestini, D. Di Castro, and G Bianconi. The strain quantum critical point for superstripes in the phase diagram of all cuprate perovskites. *International Journal of Modern Physics B*, 14(29n31):3342–3355, December 2000.
- [27] MI Salkola, AR Bishop, SA Trugman, and J. Mustre de Leon. Correlation-function analysis of nonlinear and nonadiabatic systems: Polaron tunneling. *Physical Review B*, 51(14):8878–8891, April 1995.
- [28] J. Mustre de Leon, R. de Coss, AR Bishop, and SA Trugman. Isotopic substitution in a model polaronic system. *Physical Review B*, 59(13):8359–8362, April 1999.
- [29] José Mustre de León, J Miranda Mena, and a R Bishop. Microstrain and polaronic correlation in a model system. *Journal of Physics: Conference Series*, 108:012020, March 2008.
- [30] J. Miranda Mena, J. Mustre de León, and a. R. Bishop. Effect of Uniaxial Pressure on the Isotope Effect on the Spectrum of Hamiltonians with Electron–Phonon Coupling. *Journal of Superconductivity and Novel Magnetism*, 20(7-8):603–608, September 2007.

- 
- [31] J. Miranda Mena, J. Mustre León, and a. R. Bishop. Polaron Formation in a Model Hamiltonian with Covalent Electron–Phonon Interactions. *Journal of Superconductivity*, 18(5-6):723–726, January 2006.
- [32] J. Mustre de León, R. de Coss, A. Rubio-Ponce, R. Palí, A.R. Bishop, and S.a. Trugman. Polaronic Signatures in Phonon Isotopic Shifts. *physica status solidi (b)*, 220(1):499–502, July 2000.
- [33] V. Ivanov, M. Iliev, and C. Thomsen. Micro-Raman study of isotope substitution in  $\text{YBa}_2\text{Cu}_3^{18}\text{O}_{6.2}$  during local laser annealing. *Physical Review B*, 52(18):13652–13657, November 1995.
- [34] Warren Pickett. Electronic structure of the high-temperature oxide superconductors. *Reviews of Modern Physics*, 61(2):433–512, April 1989.
- [35] R.J. Cava, B. Batlogg, K.M. Rabe, E.A. Rietman, P.K. Gallagher, and L.W. Rupp. Structural anomalies at the disappearance of superconductivity in  $\text{Ba}_2\text{YCu}_3\text{O}_{7-\delta}$ : Evidence for charge transfer from chains to planes. *Physica C: Superconductivity*, 156(4):523–527, November 1988.
- [36] J. J Capponi, C Chaillout, A. W Hewat, P Lejay, M Marezio, N Nguyen, B Raveau, J. L Soubeyroux, J. L Tholence, and R Tournier. Structure of the 100 K Superconductor  $\text{Ba}_2\text{YCu}_3\text{O}_7$  between (5 / 300) K by Neutron Powder Diffraction. *Europhysics Letters (EPL)*, 3(12):1301–1307, June 1987.
- [37] W. Schäfer, E Jansen, G Will, J. Faber, and B. Veal. Structural anomalies of  $\text{YBa}_2\text{Cu}_3\text{O}_{6.9}$  at the superconducting transition temperature. *Materials Research Bulletin*, 23(10):1439–1445, October 1988.
- [38] J. Mustre de Leon, SD Conradson, I. Batistic, and AR Bishop. Evidence for an axial oxygen-centered lattice fluctuation associated with the superconducting transition in  $\text{YBa}_2\text{Cu}_3\text{O}_7$ . *Physical Review Letters*, 65(13):1675–1678, September 1990.
- [39] S D Conradson, I D Raistrick, and a R Bishop. Axial oxygen-centered lattice instabilities and high-temperature superconductivity. *Science (New York, N.Y.)*, 248(4961):1394–8, June 1990.
- [40] P. Miceli, J. Tarascon, L. Greene, P. Barboux, F. Rotella, and J. Jorgensen. Role of bond lengths in the 90-K superconductor: A neutron powder-diffraction study of  $\text{YBa}_2\text{Cu}_{3-x}\text{Co}_x\text{O}_{7-y}$ . *Physical Review B*, 37(10):5932–5935, April 1988.



- [41] J. J. Rehr. Theoretical approaches to x-ray absorption fine structure. *Reviews of Modern Physics*, 72(3):621–654, July 2000.
- [42] George H. Kwei, Allen C. Larson, W.L. Hults, and James L. Smith. Temperature dependence of the structure of  $\text{YBa}_2\text{Cu}_3\text{O}_7$ . *Physica C: Superconductivity*, 169(3-4):217–226, August 1990.
- [43] T. Egami, B.H. Toby, S.J.L. Billinge, H.D. Rosenfeld, J.D. Jorgensen, D.G. Hinks, B. Dabrowski, M.A. Subramanian, M.K. Crawford, W.E. Farneth, and E.M. McCarron. Local structural anomaly near  $T_c$  observed by pulsed neutron scattering. *Physica C: Superconductivity*, 185-189:867–868, December 1991.
- [44] J. Mustre de Leon, S. Conradson, I. Batistić, A. Bishop, I. Raistrick, M. Aronson, and F. Garzon. Axial oxygen-centered lattice instabilities in  $\text{YBa}_2\text{Cu}_3\text{O}_7$ : An application of the analysis of extended x-ray-absorption fine structure in anharmonic systems. *Physical Review B*, 45(5):2447–2457, February 1992.
- [45] B. Battlog. Re-examination of the phase diagram in heavily-doped  $\text{La}_{2-x}\text{Sr}_x\text{CuO}_4$ . In Y Bar-Yam, T Egami, J de Leon, and A R Bishop, editors, *Lattice Effects in High- $T_c$  Superconductors: Proceedings of the Conference : Santa Fe, New Mexico, January 13-15, 1992*, pages 548–557. World Scientific, 1992.
- [46] R.P. Sharma, F.J. Rotella, J.D. Jorgensen, and L.E. Rehn. Neutron diffraction and ion-channeling investigations of atomic displacements in  $\text{YBa}_2\text{Cu}_3\text{O}_{7-\delta}$  between 10 and 300 K. *Physica C: Superconductivity*, 174(4-6):409–422, March 1991.
- [47] C. Thomsen and M Cardona. Comment on “Axial oxygen-centered lattice instabilities in  $\text{YBa}_2\text{Cu}_3\text{O}_7$ : An application of the analysis of extended x-ray-absorption fine structure in anharmonic systems”. *Physical Review B*, 47(18):12320–12321, May 1993.
- [48] E.A. Stern, M Qian, Y Yacoby, S.M. Heald, and H Maeda. Apical Cu-O bond in  $\text{YBa}_2\text{Cu}_3\text{O}_{7-\delta}$  superconductors by XAFS. *Physica C: Superconductivity*, 209(1-3):331–334, April 1993.
- [49] Ch Booth, F Bridges, Jb Boyce, T Claeson, Bm Lairson, R Liang, and Da Bonn. Comparison of local structure measurements from c-axis polarized XAFS between a film and a single crystal of  $\text{YBa}_2\text{Cu}_3\text{O}_{7-\delta}$  as a function of temperature. *Physical Review B*, 54(13):9542–9554, October 1996.

- 
- [50] J. Mustre de Leon, S D Conradson, I. Batistic, and A R Bishop. Correlation between axial-oxygen anharmonicity and  $T_c$  in  $\text{YBa}_2\text{Cu}_3\text{O}_7$  and related compounds. *Physical Review B*, 44:2422–2425, 1991.
- [51] A Bianconi. Non homogeneous Cu site structure configurations and Cu apical oxygen vibrations at the normal to superconducting transition. In Y Bar-Yam, T Egami, J de Leon, and A R Bishop, editors, *Lattice Effects in High- $T_c$  Superconductors: Proceedings of the Conference : Santa Fe, New Mexico, January 13-15, 1992*, pages 65–83. World Scientific, 1992.
- [52] P. Allen, J. Mustre de Leon, S. Conradson, and A. Bishop. Characterization of a split axial-oxygen site in  $\text{TlBa}_2\text{Ca}_3\text{Cu}_4\text{O}_{11}$  by extended x-ray-absorption fine-structure spectroscopy. *Physical Review B*, 44(17):9480–9485, November 1991.
- [53] C. Booth, F Bridges, E. Bauer, G Li, J. Boyce, T. Claeson, C. Chu, and Q Xiong. XAFS measurements of negatively correlated atomic displacements in  $\text{HgBa}_2\text{CuO}_{4+\delta}$ . *Physical Review B*, 52(22):R15745–R15748, December 1995.
- [54] H. Oyanagi, a. Tsukada, M. Naito, and N. Saini. Local structure of superconducting  $(\text{La,Sr})_2\text{CuO}_4$  under strain: Microscopic mechanism of strain-induced  $T_c$  variation. *Physical Review B*, 75(2):024511, January 2007.
- [55] C. Zhang and H. Oyanagi. Local lattice instability and superconductivity in  $\text{La}_{1.85}\text{Sr}_{0.15}\text{Cu}_{1-x}\text{M}_x\text{O}_4$  ( $\text{M}=\text{Mn}$ ,  $\text{Ni}$ , and  $\text{Co}$ ). *Physical Review B*, 79(6):064521, February 2009.
- [56] S D Conradson, J. Mustre Leon, and A R Bishop. Local phase separation in Tl-based oxide superconductors. *Journal of Superconductivity*, 10(4):329–332, August 1997.
- [57] A Lanzara, N L Saini, A Bianconi, J. L. Hazemann, Y. Soldo, F. C. Chou, and D. C. Johnston. Temperature-dependent modulation amplitude of the  $\text{CuO}_2$  superconducting lattice in  $\text{La}_2\text{CuO}_{4.1}$ . *Physical Review B*, 55(14):9120–9124, April 1997.
- [58] J Mustre de Leon, M Acosta-Alejandro, S D Conradson, and A R Bishop. Local structure fluctuations as a signature of an inhomogeneous ground state in high- $T_c$  superconductors. *Journal of synchrotron radiation*, 12(Pt 2):193–6, March 2005.

- [59] A. Bianconi, M. Lusignoli, N. Saini, P. Bordet, Å. Kvik, and P. Radaelli. Stripe structure of the  $\text{CuO}_2$  plane in  $\text{Bi}_2\text{Sr}_2\text{CaCu}_2\text{O}_{8+y}$  by anomalous x-ray diffraction. *Physical Review B*, 54(6):4310–4314, August 1996.
- [60] T. Egami and S.J.L. Billinge. *Underneath the Bragg peaks structural analysis of complex materials*. Pergamon, Kiddington, Oxford, UK; Boston, 2003.
- [61] E. Božin, S. Billinge, G. Kwei, and H Takagi. Charge-stripe ordering from local octahedral tilts: Underdoped and superconducting  $\text{La}_{2-x}\text{Sr}_x\text{CuO}_4$  ( $0 \leq x \leq 0.30$ ). *Physical Review B*, 59(6):4445–4454, February 1999.
- [62] E. Božin, G. Kwei, H Takagi, and S. Billinge. Neutron Diffraction Evidence of Microscopic Charge Inhomogeneities in the  $\text{CuO}_2$  Plane of Superconducting  $\text{La}_{2-x}\text{Sr}_x\text{CuO}_4$  ( $0 \leq x \leq 0.30$ ). *Physical Review Letters*, 84(25):5856–5859, June 2000.
- [63] S A Kivelson, I P Bindloss, V Oganessian, J. M. Tranquada, A. Kapitulnik, and C. Howald. How to detect fluctuating stripes in the high-temperature superconductors. *Reviews of Modern Physics*, 75(4):1201–1241, October 2003.
- [64] Nicola Poccia, Gaetano Campi, Michela Fratini, Alessandro Ricci, Naurang L. Saini, and Antonio Bianconi. Spatial inhomogeneity and planar symmetry breaking of the lattice incommensurate supermodulation in the high-temperature superconductor  $\text{Bi}_{-2}\text{Sr}_{-2}\text{CaCu}_{-2}\text{O}_{-8+y}$ . *Physical Review B*, 84(10):100504, September 2011.
- [65] H. Mook, Pengcheng Dai, and F. Doğan. Charge and Spin Structure in  $\text{YBa}_2\text{Cu}_3\text{O}_{6.35}$ . *Physical Review Letters*, 88(9):097004, February 2002.
- [66] J Haase and CP Slichter. Charge density variations or stripes in  $\text{YBa}_2\text{Cu}_3\text{O}_{6+y}$ . *Journal of superconductivity*, 16(3):473–475, 2003.
- [67] S H Pan, J P O’Neal, R L Badzey, C Chamon, H Ding, J R Engelbrecht, Z Wang, H Eisaki, S Uchida, A K Gupta, K W Ng, E W Hudson, K M Lang, and J C Davis. Microscopic electronic inhomogeneity in the high- $T_c$  superconductor  $\text{Bi}_2\text{Sr}_2\text{CaCu}_2\text{O}_{8+x}$ . *Nature*, 413(6853):282–5, September 2001.
- [68] M. Salkola, V. Emery, and S. Kivelson. Implications of Charge Ordering for Single-Particle Properties of High- $T_c$  Superconductors. *Physical Review Letters*, 77(1):155–158, July 1996.

- 
- [69] R. a. Fisher, J. E. Gordon, and N. E. Phillips. Specific heat of the high- $T_c$  oxide superconductors. *Journal of Superconductivity*, 1(3):231–294, September 1988.
- [70] J.W. Loram, K.A. Mirza, and P.F. Freeman. The electronic specific heat of  $\text{YBa}_2(\text{Cu}_{1-x}\text{Zn}_x)_3\text{O}_7$  from 1.6 K to 300 K. *Physica C: Superconductivity*, 171(3-4):243–256, November 1990.
- [71] J. W. Loram, K. A. Mirza, J. R. Cooper, and W. Y. Liang. Electronic specific heat of  $\text{YBa}_2\text{Cu}_3\text{O}_{6+x}$  from 1.8 to 300 K. *Physical Review Letters*, 71(11):1740–1743, September 1993.
- [72] J W Loram, K A Mirza, J R Cooper, W Y Liang, and J M Wade. Electronic specific heat of  $\text{YBa}_2\text{Cu}_3\text{O}_{6+x}$  from 1.8 to 300 K. *Journal of Superconductivity*, 7(1):243–249, February 1994.
- [73] J.W. Loram, K.A. Mirza, J.R. Cooper, and J.L. Tallon. Superconducting and normal state energy gaps in  $\text{Y}_{0.8}\text{Ca}_{0.2}\text{Ba}_2\text{Cu}_3\text{O}_{7-\delta}$  from the electronic specific heat. *Physica C: Superconductivity*, 282-287:1405–1406, August 1997.
- [74] J.W. Loram, J Luo, J.R. Cooper, W.Y. Liang, and J.L. Tallon. Evidence on the pseudogap and condensate from the electronic specific heat. *Journal of Physics and Chemistry of Solids*, 62(1-2):59–64, January 2001.
- [75] B. Bucher, P. Steiner, J. Karpinski, E. Kaldis, and P. Wachter. Influence of the spin gap on the normal state transport in  $\text{YBa}_2\text{Cu}_4\text{O}_8$ . *Physical Review Letters*, 70(13):2012–2015, March 1993.
- [76] C. Reynolds, B. Serin, W. Wright, and L. Nesbitt. Superconductivity of Isotopes of Mercury. *Physical Review*, 78(4):487–487, May 1950.
- [77] Emanuel Maxwell. Isotope Effect in the Superconductivity of Mercury. *Physical Review*, 78(4):477–477, May 1950.
- [78] K. Conder, E. Kaldis, M. Maciejewski, K.A. Müller, and E.F. Steigmeier. Oxygen isotope exchange kinetics and site-selective oxygen substitution in  $\text{YBa}_2\text{Cu}_3^{18}\text{O}_{7-\chi}$ . *Physica C: Superconductivity*, 210(1-2):282–288, May 1993.
- [79] M. Cardona, R. Liu, C Thomsen, W. Kress, E. Schönherr, M. Bauer, L Genzel, and W. König. Effect of isotopic substitution of oxygen on  $T_c$  and the phonon frequencies of high  $T_c$  superconductors. *Solid State Communications*, 67(8):789–793, August 1988.

- [80] C Thomsen, Hj. Mattausch, M Bauer, W. Bauhofer, R. Liu, L Genzel, and M Cardona. Raman and far infrared studies of  $\text{YBa}_2\text{Cu}_3\text{O}_{7-\delta}$  prepared exclusively with  $^{18}\text{O}$ . *Solid State Communications*, 67(11):1069–1072, September 1988.
- [81] A. R. Bishop, A. Bussmann-Holder, O. V. Dolgov, A. Furrer, H. Kamimura, H. Keller, R. Khasanov, R. K. Kremer, D. Manske, K. A. Müller, and A. Simon. Real and Marginal Isotope Effects in Cuprate Superconductors. *Journal of Superconductivity and Novel Magnetism*, 20(5):393–396, July 2007.
- [82] G. Ruani, C. Taliani, M. Muccini, K. Conder, E. Kaldis, H. Keller, D. Zech, and K. Alex Müller. Apex anharmonicity observed by Raman scattering in  $^{18}\text{O}$  substituted  $\text{YBa}_2\text{Cu}_3\text{O}_{6+x}$ . *Physica C: Superconductivity*, 226(1-2):101–105, June 1994.
- [83] D. Zech, H. Keller, K. Conder, E. Kaldis, E. Liarokapis, N. Poulakis, and K. A. Müller. Site-selective oxygen isotope effect in optimally doped  $\text{YBa}_2\text{Cu}_3\text{O}_{6+x}$ . *Nature*, 371(6499):681–683, October 1994.
- [84] Guo-meng Zhao, M. B. Hunt, H. Keller, and K. A. Müller. Evidence for polaronic supercarriers in the copper oxide superconductors  $\text{La}_{2-x}\text{Sr}_x\text{CuO}_4$ . *Nature*, 385(6613):236–239, January 1997.
- [85] J Hofer, K Conder, T Sasagawa, Guo-meng Zhao, M Willemin, H Keller, and K Kishio. Oxygen-Isotope Effect on the In-Plane Penetration Depth in Underdoped  $\text{La}_{2-x}\text{Sr}_x\text{CuO}_4$  Single Crystals. *Physical Review Letters*, 84(18):4192–4195, May 2000.
- [86] R. Khasanov, D. G. Eshchenko, H. Luetkens, E. Morenzoni, T. Prokscha, a. Suter, N. Garifianov, M. Mali, J. Roos, K. Conder, and H. Keller. Direct Observation of the Oxygen Isotope Effect on the In-Plane Magnetic Field Penetration Depth in Optimally Doped  $\text{YBa}_2\text{Cu}_3\text{O}_{7-\delta}$ . *Physical Review Letters*, 92(5):057602, February 2004.
- [87] D. Castro, M. Angst, D. Eshchenko, R. Khasanov, J. Roos, I. Savić, a. Shengelaya, S. Bud’ko, P. Canfield, K. Conder, J. Karpinski, S. Kazakov, R. Ribeiro, and H. Keller. Absence of a boron isotope effect in the magnetic penetration depth of  $\text{MgB}_2$ . *Physical Review B*, 70(1):1–5, July 2004.
- [88] V. Kresin and S. Wolf. Colloquium: Electron-lattice interaction and its impact on high  $T_c$  superconductivity. *Reviews of Modern Physics*, 81(2):481–501, April 2009.

- 
- [89] A Lanzara, Guo-meng Zhao, N L Saini, A Bianconi, K Conder, H Keller, and K A Müller. Oxygen-isotope shift of the charge-stripe ordering temperature in  $\text{La}_{2-x}\text{Sr}_x\text{CuO}_4$  from x-ray absorption spectroscopy. *Journal of Physics: Condensed Matter*, 11(48):L541–L546, December 1999.
  - [90] GH Gweon, T Sasagawa, S Y Zhou, J Graf, H Takagi, D-H Lee, and A Lanzara. An unusual isotope effect in a high-transition-temperature superconductor. *Nature*, 430(6996):187–90, July 2004.
  - [91] John F Douglas, Hideaki Iwasawa, Zhe Sun, Alexei V Fedorov, Motoyuki Ishikado, Tomohiko Saitoh, Hiroshi Eisaki, Hiroshi Bando, Takeshi Iwase, Akihiro Ino, Masashi Arita, Kenya Shimada, Hirofumi Namatame, Masaki Taniguchi, Takahiko Masui, Setsuko Tajima, Kazuhiro Fujita, Shin-ichi Uchida, Yoshihiro Aiura, and Daniel S Dessau. Superconductors: unusual oxygen isotope effects in cuprates? *Nature*, 446(7133):E5, March 2007.
  - [92] C. Thomsen, E. Schönherr, B. Friedl, and M. Cardona. Identification of the  $1250\text{-cm}^{-1}$  Raman feature in  $\text{YBa}_2\text{Cu}_3\text{O}_6$ . *Physical Review B*, 42(1):943–945, July 1990.
  - [93] M. DeWeert, D. Papaconstantopoulos, and W. Pickett. Tight-binding Hamiltonians for high-temperature superconductors and applications to coherent-potential-approximation calculations of the electronic properties of  $\text{La}_{2-x}\text{Ba}_x\text{CuO}_{4-y}$ . *Physical Review B*, 39(7):4235–4248, March 1989.
  - [94] Mark Hybertsen, Michael Schlüter, and Niels Christensen. Calculation of Coulomb-interaction parameters for  $\text{La}_2\text{CuO}_4$  using a constrained-density-functional approach. *Physical Review B*, 39(13):9028–9041, May 1989.
  - [95] J Demsar, B Podobnik, V. Kabanov, Th Wolf, and D Mihailovic. Superconducting Gap  $\Delta_c$ , the Pseudogap  $\Delta_p$ , and Pair Fluctuations above  $T_c$  in Overdoped  $\text{Y}_{1-x}\text{Ca}_x\text{Ba}_2\text{Cu}_3\text{O}_{7-\delta}$  from Femtosecond Time-Domain Spectroscopy. *Physical Review Letters*, 82(24):4918–4921, June 1999.
  - [96] P. Kusar, J. Demsar, D. Mihailovic, and S. Sugai. A systematic study of femtosecond quasiparticle relaxation processes in  $\text{La}_{2-x}\text{Sr}_x\text{CuO}_4$ . *Physical Review B*, 72(1):014544, July 2005.
  - [97] R Pali, A. Rubio-Ponce, R. De Coss, and J. Mustre de León. Isotope effect in anharmonic double-well potentials. *Revista Mexicana de Física*, 44(1):77–79, 1998.

- 
- [98] A. García Saravia Ortiz de Montellano and J. Mustre de León. Characterization of an Electronic Excitation on a Peierls–Hubbard Hamiltonian for a Small Cluster. *Journal of Superconductivity and Novel Magnetism*, 27(4):991–994, November 2013.
- [99] Ta Tyson, J. de Leon, Sd Conradson, Ar Bishop, Jj Neumeier, H Röder, and Jun Zang. Evidence for a local lattice distortion in Ca-doped LaMnO<sub>3</sub>. *Physical Review B*, 53(21):13985–13988, June 1996.
- [100] M. Acosta-Alejandro, J. de León, M. Medarde, Ph. Lacorre, K. Konder, and P. Montano. Local lattice structure change in PrNiO<sub>3</sub> across the metal-insulator transition: X-ray absorption near-edge structure spectroscopy and ab initio calculations. *Physical Review B*, 77(8):085107, February 2008.
- [101] H. Ding, T. Yokoya, J. C. Campuzano, T. Takahashi, M. Randeria, M. R. Norman, T. Mochiku, K. Kadowaki, and J. Giapintzakis. Spectroscopic evidence for a pseudogap in the normal state of underdoped high-T<sub>c</sub> superconductors. *Nature*, 382(6586):51–54, July 1996.
- [102] N E Hussey, M Abdel-Jawad, A Carrington, A P Mackenzie, and L Balicas. A coherent three-dimensional Fermi surface in a high-transition-temperature superconductor. *Nature*, 425(6960):814–7, October 2003.
- [103] Andrés García Saravia Ortiz de Montellano. Polarons. <https://github.com/andresgsaravia/polarons/releases/tag/1.0.0>, 2014.
- [104] Gaël Guennebaud, Benoît Jacob, and Others. Eigen. <http://eigen.tuxfamily.org>, 2010.
- [105] David Bateman and Andy Adler. Sparse matrix implementation in octave. *arXiv preprint cs/0604006*, 2006.
- [106] Octave community. GNU Octave 3.8.1. <http://www.gnu.org/software/octave/>, 2014.
- [107] R. B. Lehoucq, D. C. Sorensen, and C. Yang. ARPACK Users Guide: Solution of Large Scale Eigenvalue Problems by Implicitly Restarted Arnoldi Methods., 1997.





# List of Figures

1.1	Simplified version of the cuprate superconductor phase diagram . . .	2
1.2	Crystal structure of $\text{YBa}_2\text{Cu}_3\text{O}_7$ and the two possible O(4)-Cu(1)-O(4) configurations. . . . .	7
2.1	Schematic for the symmetric (Raman) and antisymmetric (infrared) vibrational modes in $\text{CuO}_2$ . . . . .	15
2.2	Diagram for 3 masses attached with springs representing the nuclei motion. . . . .	20
3.1	Projection into phonon coordinates (left panel) and calculated cluster distortion $d$ (right panel) for different $\lambda_{ir}$ coupling values with $u_R = 0$ . . . . .	28
3.2	Ground and first excited states projected into phonon coordinates. . .	29
3.3	Bipolaron formation energy as a function of the $\lambda_{ir}$ coupling. . . . .	30
3.4	Isotopic shift of the bipolaron formation energy. . . . .	31
4.1	Projection of the first <i>electronic</i> state with itself at $\lambda_{ir} = 0$ . . . . .	34
4.2	Infrared-active excitations as a function of electron-lattice coupling. .	36
4.3	Isotopic shifts for the different infrared excitations. . . . .	37
4.4	Projection into phonon coordinates of the states with two and three infrared phonons. . . . .	39
5.1	Energy of the electronic excitations as function of $\lambda_{ir}$ . . . . .	42
5.2	Probability of finding the system with one charge in an oxygen and the other at the copper and both charges at opposing oxygen sites. . . . .	44
5.3	Projection into phonon coordinates of the electronic excitation. . . . .	45
5.4	Isotopic shift of the electronic excitations as a function of $\lambda_{ir}$ . . . . .	46